Compositional Control of Aging Kinetics in TDP-43 Condensates

Nuria H. Espejo,[1,2,*] Alejandro Feito,[1,*] Ignacio Sanchez-Burgos,[3] Adiran Garaizar,[2] Maria M. Conde,[4] Antonio Rey,[1] Eduardo Pedraza,[1] Alejandro Castro,[1] Rosana Collepardo-Guevara,[3] Andres R. Tejedor,[1,3,‡] and Jorge R. Espinosa[1,3,†]

[1]*Department of Physical-Chemistry, Universidad Complutense de Madrid, Avenida Complutense s/n, Madrid 28040, Spain*
[2]*Data Science, Bayer AG, Alfred-Nobel-Straße 50, 40789 Monheim am Rhein, Germany*
[3]*Yusuf Hamied Department of Chemistry, University of Cambridge, Lensfield Road, Cambridge CB2 1EW, United Kingdom*
[4]*Department of Chemical Engineering, Universidad Politécnica de Madrid, C/ Jose Gutierrez Abascal 2, Madrid 28006, Spain*

(Received 17 March 2025; accepted 7 October 2025; published 11 December 2025)

The spontaneous self-assembly of proteins and nucleic acids into biomolecular condensates has been shown to ubiquitously contribute to the functional compartmentalization of the cell. However, their liquid-to-solid transformation (i.e., aging) driven by interprotein β-sheet transitions represents a hallmark of multiple neurodegenerative disorders. We perform molecular dynamics simulations to elucidate the role of different biomolecules in regulating the aging kinetics of TDP-43, an RNA-binding protein linked to amyotrophic lateral sclerosis and frontotemporal dementia. We find that while arginine-rich peptides accelerate the nucleation of interprotein β-sheet structures, the inclusion of RNAs and the HSP70 chaperone slows down their emergence. Interestingly, we observe a correlation between the protein compactness—governed by the condensate composition—and aging kinetics. Moreover, we find that near-interfacial regions of TDP-43 condensates exhibit faster interprotein transitions than the core of the condensate. Together, our findings underscore the major role of client biomolecules in controlling the propensity of multicomponent condensates to form harmful solidlike states.

DOI: 10.1103/w7g3-6rsd

I. INTRODUCTION

TAR DNA-binding protein 43 (TDP-43) is a multidomain protein located in the cell nucleus involved in RNA metabolism. The RNA recognition motifs (RRM) located in the central part of TDP-43 enable effective binding to RNA and DNA sequences facilitating the formation and regulation of multicomponent membraneless compartments [1]. Under physiological conditions, TDP-43 orchestrates essential functions including RNA metabolism, transcriptional regulation, and stress response pathways [1–3]. However, TDP-43 dysfunction and cytosol mislocalization are hallmarks of several neurodegenerative disorders, most notably amyotrophic lateral sclerosis (ALS) and frontotemporal dementia (FTD), where cytoplasmic accumulation of TDP-43 aggregates correlates with disease progression [4–9]. The biomolecular assemblies formed by TDP-43 exhibit complex viscoelastic properties that range from highly dynamic, liquidlike states to more rigid, gellike or solidlike configurations [10–14]. In that respect, the partly helical region in TDP-43 low-complexity domain (LCD)—which contributes to its propensity to aggregate under pathological conditions [2,5]—harbors almost all of the TARDBP gene mutations identified in neurodegenerative disorders [4,15]. Importantly, different biomolecules such as polypeptide repeats [16–19] or RNAs [20–22] can strongly modulate the phase behavior of TDP-43 condensates. Particularly, arginine-rich dipeptide repeat (DPR) proteins, such as poly-GR and poly-PR, are abundant in patients with ALS or FTD and have been revealed to promote phase separation and insolubility of TDP-43 *in vitro* [16,23–25] and *in vivo* [18,26]. These peptides predominantly form cytoplasmic inclusions in the brains of patients with ALS or FTD [19,26,27] and are related to a large repeat expansion of hexanucleotides in the C9orf72 gene [28–30]. In contrast, specific RNA sequences (e.g., enriched in uridine and adenosine) have been identified to bind to TDP-43 in stress granules, reducing its accumulation in the cytoplasm and potentially stabilizing its liquidlike state, preventing harmful aggregation [20,21,31]. Furthermore, chaperones, which often display a high binding affinity to proteins that scaffold biomolecular condensates, promote dynamic regulation of condensate stability, including modulation of their saturation concentration (C_{sat}) and inhibition of pathological phase transitions [32,33]. For instance, the heat shock protein 70 (HSP70) plays a critical role in disassembling aged stress granules containing misfolded proteins such as SOD1 [34] or TDP-43 [35]. Hence, while it is known that diverse biomolecules can substantially regulate the phase behavior of RBPs such as TDP-43, the precise mechanism at the molecular level by which each individual species dictates the material properties, internal organization, and stability of protein condensates, remains elusive.

*These authors contributed equally to this work.
†Contact author: jorgerene@ucm.es
‡Contact author: at949@cam.ac.uk

Experimental techniques such as microrheology and fluorescence recovery after photobleaching (FRAP)—involving bead-tracking and optical tweezers [36–42]—have demonstrated the temporal evolution of protein [43,44] and RNA [45] condensates toward kinetically arrested states [12,46–50]. However, elucidating the intricacies of binding/unbinding events and intermolecular forces underlying these transitions remains still challenging for experimental approaches at sub-molecular resolution [51,52]. Computer simulations, either atomistic [53–58] or coarse-grained [59–62], provide a powerful framework to achieve such resolution and characterize the interactions and mechanisms controlling condensate's phase behavior [63–68]. While previous computational studies have been primarily focused on amyloid formation in small peptides and isolated domains [69–71], fewer investigations have addressed the molecular mechanisms governing material state transitions in multicomponent biomolecular condensates [72–74]. Understanding the different governing parameters that control aging is essential to propose effective strategies to modulate biomolecular condensates' material properties and prevent transitions toward potentially pathological solidlike assemblies.

In this work, we investigate the phase behavior of multicomponent condensates where TDP-43 acts as the main scaffold protein. We examine how the stability, internal architecture and aging kinetics of TDP-43 condensates are regulated by the inclusion of three types of biomolecules: arginine-rich polypeptides, single-stranded disordered poly-Uridine RNA, and the HSP70 chaperone. We use the sequence-dependent Mpipi-Recharged model [75], a residue-resolution coarse-grained model that incorporates improved treatment for electrostatic interactions [58,75–77] while maintaining computational efficiency through implicit solvation. We first benchmark the performance of the model to describe single-molecule properties of TDP-43, as well as higher-order self-assembly of pure TDP-43 condensates and binary mixtures of arginine-rich polypeptides with TDP-43. After validating the model for these systems, we combine equilibrium and nonequilibrium simulations of TDP-43 multicomponent condensates to elucidate the impact of the aforementioned biomolecules in regulating the propensity of TDP-43 to form interprotein β-sheet structures. We find that while arginine-rich polypeptides increase the nucleation rate of cross-β-sheet structures—consistent with experimental observations [18,27]—the presence of poly-Uridine RNA and HSP70 substantially decelerates the progressive formation of cross-β-sheet clusters. Interestingly, we also detect that interprotein β-sheet transitions occur faster in condensates coexisting with the dilute protein phase, which display an interface, than in the bulk of the condensate. This behavior is ascribed to the relative ratio of inter- versus intramolecular contacts that aggregation-prone domains (i.e., the LCD of TDP-43) establish depending on the precise condensate biomolecular region and surrounding physicochemical environment. Collectively, our findings establish a direct link between the effects of different biomolecular species on TDP-43 intermolecular contacts and the condensate's propensity to form cross-β-sheet clusters and undergo transitions toward aberrant solidlike states.

II. RESULTS

A. Residue-resolution coarse-grained modeling of TDP-43 phase separation

We simulate TDP-43 using the Mpipi-Recharged model [75], a coarse-grained force field in which each amino acid is represented by a single bead with its own chemical identity. The intrinsically disordered regions of TDP-43 are considered fully flexible polymers, in which subsequent amino acids are connected by harmonic bonds, while the globular domains are treated as rigid bodies, [75] preserving the structures taken from the corresponding protein data bank (PDB). The different residue-residue interactions in the model consist of a combination of electrostatic and hydrophobic interactions [61,78] implemented through a Yukawa potential and a Wang-Frenkel potential [79], respectively (further details of the model can be found in the Supplemental Material (SM) Sec. SI [80]). Importantly, the Yukawa potential permits the parameters to be fine-tuned depending on the specific charged residue pair. Such modification with respect to previous models allows the Mpipi-Recharged to consider that, at a coarse-grained level, the asymmetrical description of attraction and repulsion should compensate for the loss of explicit ions and water, as well as for the aggressive mapping of the many charges that an amino acid carries atomistically, reducing it to just one charge centered on its α carbon when coarse-grained.

As an initial benchmark for modeling TDP-43, we compare the single-protein radius of gyration (R_g) predicted by the Mpipi-Recharged model against atomistic calculations [13] and *in vitro* experimental values under diluted conditions [81]. The protein architecture of TDP-43 [Fig. 1(a)] consists of a partially ordered N-terminal domain (NTD and NLS), followed by two well-folded DNA/RNA-binding domains (RRM1 and RRM2) and a C-terminal domain. The C-terminal domain is composed of a low-complexity domain rich in glycine residues and IDRs, along with a conserved region (CR) that forms an α-helical structure [Fig. 1(a)] [4]. A nuclear localization signal (NLS) [84] makes it predominantly located in the nucleus, shuttling between the nucleus and the cytoplasm to perform its functions [4,13]. The determination of R_g (see Sec. SIV in the SM for further details [80]) provides structural insights into the dynamic conformations that the protein can establish depending on its environment (e.g., solvated in an aqueous solution or in a protein condensed phase). In Fig. 1(b), the R_g probability distribution [P(R_g)] of TDP-43 under diluted conditions (dashed curve) predicted by the Mpipi-Recharged model is represented along with the mean value of R_g from atomistic simulations [13] [pink vertical line; Fig. 1(b)] and *in vitro* measurements [81] [purple vertical line; Fig. 1(b)]. The mean value of R_g predicted by our model ($R_g = 36.2 \pm 1$ Å) closely agrees with the experimental value of $R_g = 41$ Å at physiological conditions (i.e., T=298 K and 150 mM of NaCl) and matches the atomistic simulation value ($R_g^{\mathrm{Atom}} = 35.6 \pm 1$ Å) within the uncertainty. Please note that the experimental measurements were performed on the mutant WtoA of TDP-43 to facilitate the SAXS measurements [81], and the solution conditions (including complex buffers compositions) differ from our simulation setup. However, the conformational ensemble of TDP-43 should not

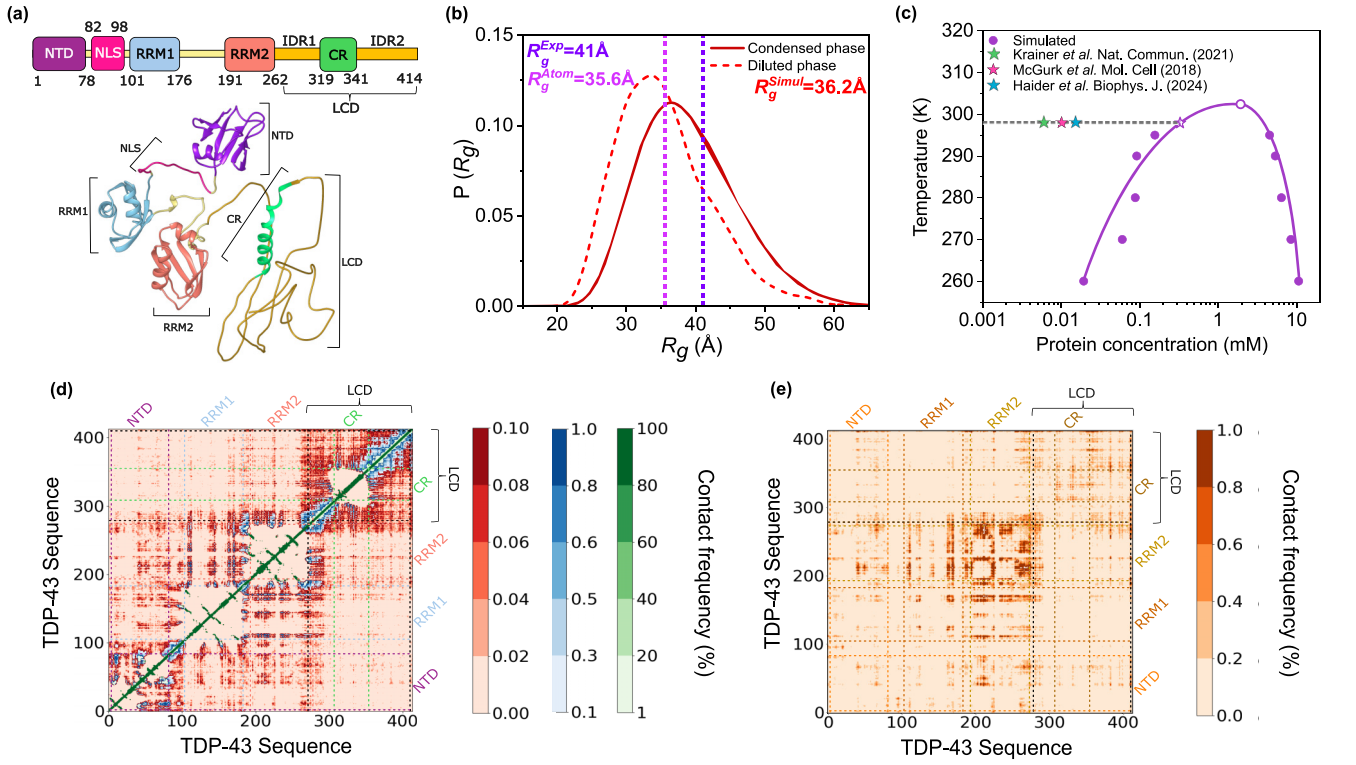

FIG. 1. (a) TDP-43 protein sequence broken down in its different domains. It consists of an N-terminal domain (NTD), a nuclear localization signal (NLS), two DNA/RNA binding domains (RRM1 and RRM2) connected by flexible linkers, and a glycine rich C-terminal domain where there is a low-complexity domain (LCD) formed by two intrinsically disordered regions (IDR1 and IDR2) and a conserved region (CR) formed by a α-helical structure [13]. The structure of the different globular domains (PDB codes: 5MDI for NTD; 2CQG for RRM1; 1WF0 for RRM2; and 2N2C for CR) across the sequence is shown in the bottom panel (further details on TDP-43 structure are provided in Sec. SIII of the SM [80]). (b) Probability distribution of the radius of gyration (R_g) of TDP-43 within the condensate (continuous line) and in the diluted phase (dashed one) at 300 K and physiological salt conditions. The single-molecule mean value of R_g from *in vitro* measurements of a TDP-43 mutant [81] and atomistic simulations of TDP-43 [13] at diluted conditions, T = 300 K and NaCl 150 mM, are depicted by vertical purple and pink dashed lines, respectively. (c) Phase diagram of TDP-43 in the temperature–concentration plane obtained via direct coexistence simulations along with the experimental C_{sat} values experimentally determined (green, pink and blue stars) from Refs. [20,82,83]. The gray dashed lined indicates the experimental temperature, and its intersection with the simulated curve defines our corresponding simulated C_{sat} value (purple empty star). (d) Intramolecular contact frequency map of residue-residue interactions (in %) of TDP-43 at diluted conditions. The different domains are indicated by vertical and horizontal dashed lines. (e) Intermolecular contact frequency map of pairwise residue interactions (in %) of TDP-43 within a protein condensate.

substantially vary with respect to the wild-type sequence upon that specific mutation and the employed solution conditions. We have also computed the probability distribution of TDP-43 R_g within the condensate at the same conditions [Fig. 1(b), red continuous curve]. TDP-43 displays larger R_g values in the condensate compared to the diluted phase due to stabilization of intermolecular contacts among different protein chains in more extended conformations with respect to the more compact conformations that single proteins exhibit in diluted conditions. This result is consistent with prior computational [85,86] and experimental studies [87], which reported more extended conformations for various IDPs within condensates compared to dilute conditions. Such conformations arise to maximize the intermolecular connectivity, thereby enhancing the enthalpic gain associated with the formation of a condensed liquid network.

To determine the conditions that enable TDP-43 condensate formation as predicted by the Mpipi-Recharged model, we calculated its phase diagram in the temperature–concentration plane [Fig. 1(c)]. The critical solution temperature (T_c) resulting for TDP-43 condensate from our direct coexistence (DC) simulations—estimated by means of the law of rectilinear diameters and critical exponents (see Sec. SV of the SM for details of this calculation and inherent limitations of the method [80])—is $T_c = 302 \pm 5$ K. Below this temperature, a protein-poor liquid phase coexists with a protein-rich condensed phase, as observed in our simulations at 290 K or 295 K, in contrast to the single homogeneous phase seen at 305 K (see Fig. S7 in the SM [80]). We compare our calculated coexistence line with *in vitro* saturation concentration values (C_{sat}) to undergo phase separation under physiological salt conditions [20,82,83] [colored stars in Fig. 1(c)]. The small differences between the three experimental values (e.g., from 0.002 to 0.01 mM) are possibly ascribed to variations in the solution NaCl concentration (e.g., 50 mM instead of 150 mM as in Ref. [83]) or sequence modifications (C_{sat} in Ref. [82] refers to TDP-43 LCD, and in Ref. [20] to a His6-SUMO N-terminally tagged TDP-43-WT). Regarding

the predicted C_{sat} value from the Mpipi-Recharged model, we note that it significantly overestimates experimental saturation concentrations over a factor of ∼30 ($C_{sat}^{\text{Mpipi-Recharged}} = 0.15 \pm 0.05$ mM). This discrepancy can be attributed to several factors: (1) model deficiencies in approximating the coarse-grained intermolecular interactions; (2) the uncertainty in C_{sat} evaluation via DC simulations (which can be up to a fivefold) due to the challenge of accurately determining extremely low protein concentrations in the diluted phase [76,78,88]; and (3) C_{sat} is a subtle quantity which can vary by few orders of magnitude depending on specific thermodynamic conditions, sequence modifications or buffer solution, hence slight variations on these conditions between experiments and simulations can lead to sensitive differences in the saturation concentration [44,89]. Therefore, given these considerations and the inherent uncertainty of our calculations and limitations of the model, the observed differences fall within the expected ranges for this type of comparison.

Once benchmarked the model performance in describing single-molecule properties and higher-order self-assembly of TDP-43 condensates, we elucidate the key molecular contacts that dictate the structural behavior of TDP-43 at diluted conditions, as well as within phase-separated condensates. To that purpose, we consider a pairwise contact when two residues (either of the same molecule, i.e., intramolecular, or between different proteins, e.g., intermolecular) are found at a distance below $1.2\sigma_{ij}$, being σ_{ij} the average molecular diameter of the two residues i and j, and 1.2 a slightly larger distance to the minimum in the interaction potential ($\sim 1.12\sigma_{ij}$) between the ith and jth amino acids (further details on these calculations are provided in Sec. SVI in the SM [80]). This criterion ensures significant residue binding and avoids artificial contacts that do not actually contribute to the condensate stability and enthalpic gain. At intramolecular level [Fig. 1(d)], there are two well-defined regions that exhibit a substantial number of contacts: (i) a large domain corresponding to several globular subregions across the sequence (i.e., NTD, RRM1, and RRM2), and (ii) the most representative segment corresponding to the low-complexity domain [IDR1, CR, and IDR2, please refer to Fig. 1(a)]. The LCD (residues 267–414) is characterized by a repetitive and low-complexity amino acid sequence that favors the formation of intramolecular interactions, and it has been suggested to contribute to TDP-43's propensity to undergo phase separation and subsequent aberrant solidification [15,90–95]. Our simulations show that the LCD tends to self-organize and establish significant interactions within the same TDP-43 molecule [Fig. 1(d)], largely due to its intrinsically disordered nature and high aromatic composition [85,96]. In a different level, the intermolecular contact map of TDP-43 [Fig. 1(e)] reveals substantial interaction hotspots (in darker colors) that potentially enable the formation of condensates. The most representative region includes self-interactions of the RRM2 DNA/RNA binding domain of TDP-43 followed by RRM1-RRM2 and LCD-LCD contacts.

It has been recently shown that the RRM1 partially unfolds in the condensate leading to solvent exposure of cysteine 173 and 175 favoring intermolecular disulfide bond formation, and thereby lowering the minimum concentration of TDP-43 molecules needed to undergo phase separation [97]. While in our CG simulations the partial unfolding of this domain cannot be observed due to the rigid treatment of the globular domains, our simulations capture the high molecular connectivity of the RRM1 in TDP-43. In fact, besides the high contact frequencies within the RRM1 region, the RRM2 displays even higher frequency due to a specific tryptophan in the sequence (Trp-172) which facilitates such strong interconnectivity (please see the protein sequence in Sec. SIII in the SM [80]). The Trp-172 is one of the TDP-43 exposed tryptophans responsible for the modulation of its toxicity [81,98]. Importantly, although the phase modulation of TDP-43 is primarily supported by RRM1 and RRM2 interactions, the LCD of TDP-43 ranks as the second major domain in terms of establishing the highest intermolecular contact frequency [Fig. 1(e)]. Specifically, there are three tryptophan residues (Trp-334, Trp-385, and Trp-412) involved in condensate stabilization (as reported in Ref. [96]) which form multivalent connections among themselves and with other aromatic and positively charged residues across the sequence [Fig. 1(e)]. Moreover, additional aromatic residues within the LCD, such as Tyr-374, Phe-397, and Phe-401, significantly contribute to condensation-stabilizing interactions through the formation of π-π contacts. This would support recent findings regarding the pivotal role for Phe-Gly motifs of TDP-43's prionlike domain in creating the fibril core [99]. By performing this contact analysis at different temperatures (Fig. S4 in the SM [80]), it can be observed how the fingerprint of both intra- and intermolecular interactions is marginally affected. However, the variation in condensate density when modifying the temperature [Fig. 1(c)] shows a notable dependency on the total number of inter- and intramolecular contacts (Figs. S4(C) and S4(F) in the SM [80]), particularly near the critical point ($T = 300\ K$) where the decrease in the number of contacts is more pronounced. Together, our contact analysis, single-molecule conformational study and phase diagram demonstrate that, despite being a CG model, the Mpipi-Recharged fairly reproduces key experimental features of TDP-43 phase behavior.

B. Arginine-rich peptides and near-interfacial condensate regions enhance interprotein β-sheet structural transitions

The propensity of TDP-43 to undergo phase separation and further β-sheet fibril formation has been shown to be strongly regulated by the presence of different biomolecules, including RNA strands of different lengths [31], or short arginine-rich peptides with varying compositions [16,17,21,100]. To elucidate the key intermolecular forces controlling this behavior, we first investigate how different dipeptide repeats—GP_{25}, GR_{25}, and PR_{25}—modulate the stability of TDP-43 condensates as a function of their concentration. We define the critical solution temperature for phase separation (T_c) as our metric for biomolecular condensate stability [77] when comparing between different protein/peptide systems. Since imposing a concentration of peptides within a protein condensate is hardly attainable through DC simulations [101], we calculate the critical solution temperature by performing NpT simulations for protein/peptide mixtures, so that T_c is estimated to be between the highest temperature at which the condensate is stable (i.e., usually $\rho > 0.1\ \text{g/cm}^3$) at $p = 0$ (i.e., we

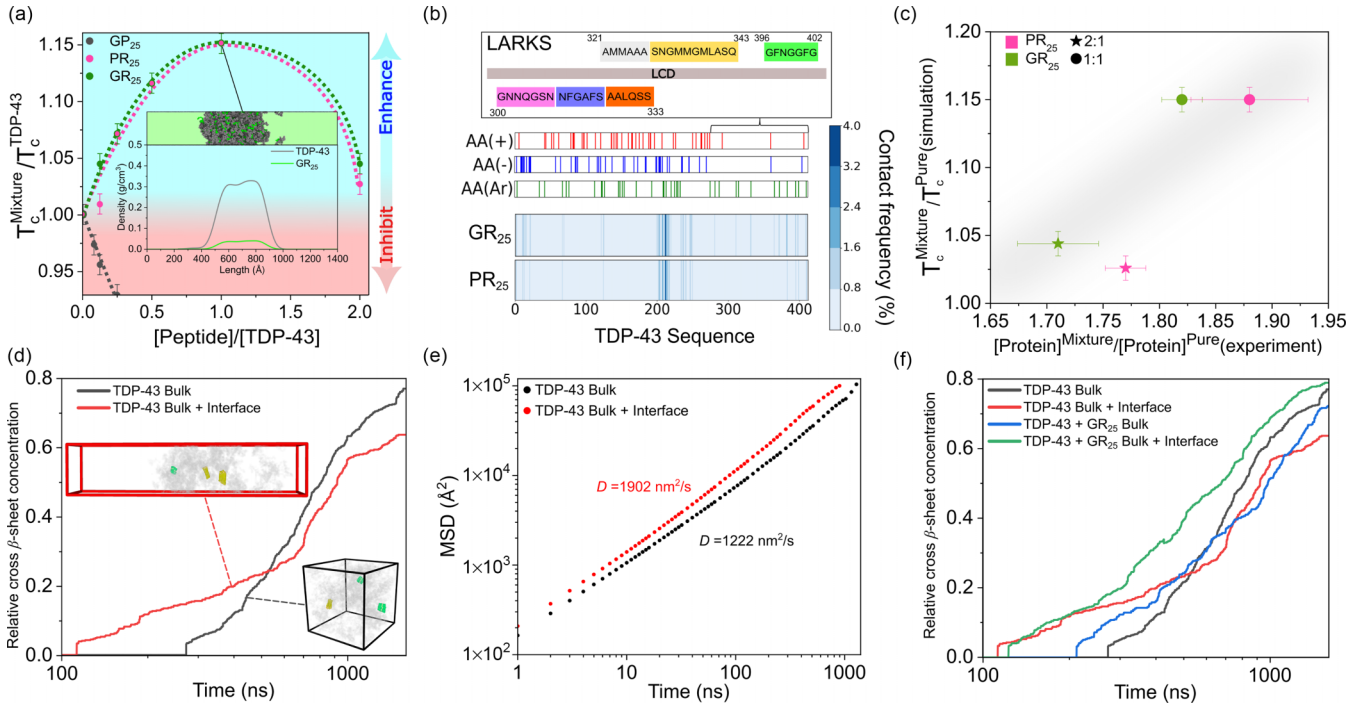

FIG. 2. (a) Relative variation in the critical solution temperature as a function of the peptide/TDP-43 molar ratio for different inserted peptides as indicated in the legend. The blue-shaded area indicates phase-separation enhancement while the red one phase-separation hindrance. Inset: Density profile of a direct coexistence simulation of GR_{25} and TDP-43 at 1:1 molar ratio depicting the relative density of each specie across the condensate. (b) Top: Low-complexity aromatic-rich kinked segments (LARKS) located at the TDP-43 LCD. Bottom: Intermolecular contact frequency map (in %) of GR_{25} and PR_{25} with the TDP-43 sequence (414 residues) in each binary mixture at 1:1 molar ratio and 300 K. The identity of charged and aromatic residues across the TDP-43 sequence are indicated above. (c) Ratio of the critical solution temperature of the binary mixture over that of pure TDP-43 condensates from Mpipi-Recharged simulations (y axis) vs *in vitro* [16] TDP-43 relative concentration within the condensates in peptide-protein mixtures over pure TDP-43 condensates (x axis). Each color corresponds to the type of peptide used and the symbol shape corresponds to peptide:protein molar ratio. (d) Time-evolution of the cross-β-sheet relative concentration in TDP-43 condensates under bulk conditions (black curve) and within condensates in coexistence with the protein-poor diluted phase (i.e., direct coexistence simulation; red curve). Snapshots of both simulation setups are displayed: protein residues forming cross-β-sheet clusters are highlighted while the rest of the protein residues within the condensate are faded in gray. (e) Mean-squared displacement (MSD) of TDP-43 proteins in the systems shown in panel (d) computed before the emergence of cross-β-sheet transitions. The diffusion coefficient (D) extracted from this analysis is also included. (f) Time-evolution of the relative cross-β-sheet concentration of pure TDP-43 condensates under bulk conditions (black curve), within condensates in coexistence with the protein diluted phase (red curve), and for (1:1) TDP-43 + GR_{25} mixtures in bulk conditions (blue) and in coexistence to the diluted phase (green).

neglect the pressure of the diluted phase on the condensate) and the lowest one at which the condensed phase evolves into the diluted phase by diverging the volume in our simulation ($\rho \lesssim 0.1\,\mathrm{g/cm^3}$, further details on this method are provided in Sec. SVa in the SM [80]). This approach—validated for biomolecular condensates in Ref. [101]—additionally allows for the evaluation of the condensate density as a function of temperature for different peptide sequences and specific RNA/protein/peptide stoichiometries.

We evaluate the stability of TPD-43 condensates as a function of the GP_{25}, GR_{25}, and PR_{25} concentration in Fig. 2(a). While both GR_{25} and PR_{25} peptides enhance the stability of the condensates up to molar ratios of $\sim$1, the inclusion of GP_{25} consistently hinders condensate formation even at relatively low concentrations (i.e., a molar ratio of 0.25). This is attributed to the strong interactions between the positively charged arginine-rich peptides (GR_{25} and PR_{25}) with the negatively charged and aromatic residues of the TDP-43 sequence. However, as we keep increasing the concentration of both GR_{25} and PR_{25} peptides, we observe a re-entrant phase behavior characterized by a nonmonotonic dependence of the condensate stability on peptide concentration: stability first increases, reaches a maximum at peptide/protein molar ratios approaching 1:1, and then it decreases at higher concentrations. This behavior emerges because while moderate peptide concentrations enhance condensate formation through complementary electrostatic interactions with TDP-43, excess of either GR_{25} or PR_{25} leads to strong peptide-peptide electrostatic self-repulsion which ultimately destabilizes the condensates. This behavior is consistent with previous experimental findings for complex coacervates of RNA-binding proteins in the presence of charged polypeptides [16,18,27]. Similar nonmonotonic changes in the stability of multicomponent condensates have also been reported for mixtures of FUS-LCD and hnRNPA1-LCD [102], and mixtures of PRC1 and RING1B [103]. Furthermore, complex coacervates consisting of short positively charged synthetic peptides (SR8 and RP3) and single-stranded RNA poly-Uridine (polyU)

[104], as well as RNA-binding proteins (such as EWSR1, TAF15, hnRNPA1, and FUS) in presence of polyU exhibit an RNA-concentration dependent re-entrant phase transition controlled by the balance between heterotypic associative electrostatic interactions and self-repulsive homotypic electrostatic interactions. In contrast to such reentrant phase behavior, GP_{25} inhibits the formation of condensates even at low concentrations since glycine and proline, which are both uncharged nonpolar residues, can only act as "spacers" [89], and poorly contribute to forming condensate-stabilizing contacts.

To further characterize the mechanism by which GR_{25} and PR_{25} modulate TDP-43 phase behavior, we carry out DC simulations to determine the internal organization of the different components within the droplets (please see Sec. SV in the SM [80]). We find that at the concentration that maximizes condensate stability (i.e., molar ratio of 1), arginine-rich peptides remain homogeneously distributed through the condensate core with a marginally low concentration at the interface (Fig. 2(a) inset). This condensate architecture differs from that previously observed in FUS/polyU mixtures where short molecules (e.g., RNA strands of 50 nucleotides) were predominantly localized at the condensate interface [101]. In this regard, the strength of the electrostatic and cation-π interactions between TDP-43 and the arginine-rich peptides underpins their retention in the condensate bulk—to maximize the enthalpic gain and the liquid network intermolecular connectivity—rather than their co-localization at the interface. In Fig. S5 in the SM [80], we show how TDP-43 + GR_{25} 1:1 mixtures maintain a similar condensate organization when the temperature is increased from 280 K to 298 K, demonstrating that despite temperature modulates the strength of the intermolecular interactions, the internal architecture of the condensates barely changes across the studied range of temperature when T is below the critical saturation concentration.

To understand which specific intermolecular interactions promote the assembly of the condensate upon the recruitment of arginine-rich peptides, we now calculate the contact frequency of GR_{25} and PR_{25} peptides with the amino acid sequence of TDP-43 [Fig. 2(b)]. Interestingly, most heterotypic contacts between these peptides and TDP-43 occur through the RRM2 domain due to its strong abundance of negatively charged and aromatic residues. Moreover, the negatively charged residues contained in the NTD and the aromatic residues within the LCD—identified as the key region driving the pathological aggregation of TDP-43 [105–110]—contribute to the condensate intermolecular connectivity in presence of arginine-rich peptides. In that respect, recent experimental evidence has shown that arginine-rich peptides bind to regions adjacent to the LCD (e.g., the RGG domains in the FUS protein), enhancing protein aggregation by increasing the LCD local concentration and its subsequent interprotein stacking [111]. A qualitative comparison between our computational predictions for the regulation of TPD-43 condensation in presence of GR_{25} and PR_{25} peptides against *in vitro* results [16] is shown in Fig. 2(c). Our model predicts the experimental observation that the 2:1 peptide/TDP-43 molar ratio translates into lower phase separation capacity (measured through the relative ratio of $T_{c,\mathrm{mixture}}/T_{c,\mathrm{TDP-43}}$ in our simulations and experimentally through the relative protein TDP-43 concentration within the condensates in absence versus presence of peptides) than the 1:1 stoichiometry. Moreover, the Mpipi-Recharged predicts the similar impact that both GR_{25} and PR_{25} induce on TDP-43 condensate stability [Figs. 2(a) and 2(c)]. At a 1:1 stoichiometry, both peptides increase protein density within the condensates in both simulations and experiments. This increase is more pronounced compared to stoichiometries in which the peptide concentration is doubled (2:1) or compared to pure TDP-43 condensates. These results indicate that our model provides a reasonable representation of the effects of short peptide recruitment on TDP-43 condensate phase behavior.

To elucidate the impact of arginine-rich peptides in TDP-43 aging kinetics, we now perform nonequilibrium MD simulations incorporating our aging algorithm. In particular, our approach enables structural transitions of the low-complexity aromatic-rich kinked segments (LARKS) [15,112] into cross-β-sheet assemblies [74,113]. As input for the free-energy binding difference between the structured versus disordered LARKS, we use atomistic potential-of-mean-force (PMF) calculations from Refs. [53,73,74,113]. In these studies, the unbinding of cross-β-sheet clusters is evaluated based on the structures of Refs. [15,112], resolved via Cryo-Electron Microscopy (Cryo-EM). PMF calculations are performed using an atom-level force field [114] which considers both structured conformations from Cryo-EM [15,112] and intrinsically disordered ensembles from all-atom simulations [114] to compute the binding free energy difference of the structured versus disordered state of a cluster composed of 4 to 6 LARKS. Our aging algorithm evaluates LARKS high-density fluctuations throughout the simulation using a distance criterion based on a local order parameter developed by us [53]. When at least five LARKS from different protein replicas meet specific proximity conditions (i.e., within a cut-off distance consistent with the free energy minima of the PMF calculations), the interactions between these segments are approximated according to the PMF structured binding free energy of the previously studied sequences [53,73,74,113]. Structured cross-β-sheet interactions are substantially stronger than LARKS disorderedlike interactions (i.e., 3-6 k_BT per LARKS when disordered and 30-50 k_BT upon the structural transition [74]). Furthermore, in addition to the energetic implications of the structural transition, our algorithm also imposes an angular potential between consecutive LARKS residues to account for the increased rigidity of the newly formed structures, thus mimicking the conformational change across the involved segment.

It is important to note that our algorithm modulates the probability of primary nucleation events solely through a distance-based criterion—specifically, by detecting local density fluctuations of LARKS. This is achieved by applying effective structural transitions to groups of chains to promote the initial formation of a cross-β-sheet nucleus. Once a cross-β-sheet cluster has formed, the algorithm facilitates interprotein β-sheet growth by adjusting the criterion to recruit additional LARKS to the existing nucleus. In contrast, secondary nucleation events are an emergent property of the system, arising spontaneously from the intrinsic fluctuations and attachment kinetics of LARKS onto preexisting cross-β-sheet clusters, and are not directly biased by the algorithm. To

avoid introducing bias in the balance between primary versus secondary nucleation rates, and assuming that the limiting step is the primary nucleation, we focus our analysis on the average nucleation time corresponding to the formation of the first cross-β-sheet nucleus, rather than the average time required for half of the TDP-43 LARKS to become engaged in cross-β-sheet structures. In this way, we establish a simplified and controlled baseline for assessing how different biomolecular species, each with distinct sequence features, influence the nucleation stage of cross-β-sheet emergence within TDP-43–scaffolded condensates. The TDP-43 LARKS considered [15] in our coarse-grained simulations are displayed in Fig. 2(b) (Top panel). For technical details on the implementation of the aging algorithm, please see Sec. SVII of the SM [80].

We measure the concentration of cross-β-sheets (normalized by the maximum number of cross-β-sheets which can be formed) in pure TDP-43 condensates as a function of time [Fig. 2(d)]. We average 5 different independent trajectories (i.e., with a different initial velocity distribution per trajectory) using two different setups. First, we employ NVT simulations at the equilibrium condensate density at 280 K [black curve in Fig. 2(d)] to emulate bulk condensate conditions below the critical solution temperature. Then, at the same temperature, we perform DC simulations (5 independent trajectories) to represent a condensate that coexists with the protein diluted phase [red curve in Fig. 2(d)], and thus they account for the presence of an interface in the condensate. We find that the presence of condensate interfaces reduces the nucleation time—i.e., defined as the average initial lag time for the formation of the first β-sheet nucleus—compared to condensate bulk conditions [Fig. 2(d)]. While we do not observe a substantially higher probability of cross-β-sheet formation at the condensate interfacial regions in our DC simulations (when tracking the position of the formed β-sheet nuclei), we consistently find that the nucleation rate is two times faster in condensates in coexistence with the dilute phase than in those under bulk conditions. Hence, our simulations suggest that interfacial (or near-interfacial) regions in TDP-43 condensates may facilitate high-density local-order fluctuations driving LARKS β-sheet structural transitions. Interestingly, these observations for TDP-43 condensates are consistent with previous experimental and computational findings for other RNA-binding proteins such as FUS [43,53], α-synuclein [115] or hnRNPA1 [116,117], which have been observed to undergo enhanced β-sheet fibrillization at the condensate boundaries. In fact, recent *in vitro* experiments [97] have reported a liquid-to-solid transition of TDP-43 in G3BP1-RNA stress granules promoted by intra-condensate demixing and TDP-43 relocation to the interface. It is important to note that, while our coarse-grained condensates undergo cross-β-sheet transitions within timescales of the order of hundreds of nanoseconds rather than in minutes to hours as experimentally observed [118], they still qualitatively capture differences in the nucleation and growth of cross-β-sheets in incubated condensates [100,118].

To further explore the origin of faster interprotein β-sheet transitions at the interfaces than in bulk conditions, we also evaluate the mean-squared displacement (MSD) (see Sec. SVIII in the SM for further details [80]) of TDP-43 proteins in condensates at bulk conditions and within DC simulations [excluding the marginal number of proteins that for a period of time transitioned from the condensate to the diluted phase; Fig. 2(e)]. We observe a moderately larger diffusion coefficient (D) for TDP-43 in condensates with interfacial regions compared to bulk systems, despite similar (though slightly slower at the interface) protein densities. This faster dynamics of TDP-43 in condensates coexisting with the diluted phase may contribute to their faster aging kinetics. Moreover, in addition to faster protein diffusion, the high-density local fluctuations of the protein LCDs (as recently reported by us for FUS condensates [43,53]) and the more extended LCD conformations—displaying a higher ratio of inter- versus intramolecular contacts (as discussed in Sec. II E)—found in condensates coexisting with the diluted phase are likely important contributors to facilitating interprotein structural transitions that form cross-β-sheet clusters. As for the aging kinetics, the diffusion coefficients calculated in our simulations are significantly faster than those experimentally found in protein condensates. Our D values are of the order of 10^3 nm^2/s, while experimental studies using FCS [119] or FRAP [38] have reported diffusion coefficients of the order 1–10 μm^2/s. Hence, the dynamics of our coarse-grained model are 3–4 orders of magnitude faster than *in vitro* measurements due to the implicit treatment of the solvent and the coarse-graining of protein residues into spherical single-interaction beads.

Next, we analyze the impact of arginine-rich peptide inclusion in TDP-43 aging kinetics. For that purpose, we measure the time-evolution of cross-β-sheet clusters in TDP-43/GR$_{25}$ condensates at 1:1 stoichiometry [Fig. 2(f)]. We choose this concentration since, as shown in Fig. 2(a), it maximizes the stability of the condensates. Moreover, given that both GR$_{25}$ and PR$_{25}$ establish a similar pattern of intermolecular contacts with TDP-43 [Fig. 2(b)], and affect similarly its phase behavior as a function of their relative concentration [Fig. 2(a)], we only perform simulations for the GR$_{25}$ peptide sequence. We consistently find (for the two sets of five different independent trajectories using both bulk NVT condensate simulations and DC simulations) that condensates with interfaces [i.e., DC setup; green curve in Fig. 2(f)] exhibit faster cross-β-sheet nucleation than condensates in bulk conditions [blue curve in Fig. 2(f)]. Furthermore, if we compare pure TDP-43 condensates versus TDP-43/GR$_{25}$ mixtures under bulk conditions, we observe that the presence of GR$_{25}$ not only promotes phase separation, but also accelerates cross-β-sheet formation. Nevertheless, such effect is negligible in the presence of interfaces where both pure TDP-43 and TDP-43/GR$_{25}$ exhibit similar nucleation times (red and green curves, respectively). We hypothesize that such different behavior in bulk conditions can be driven by GR$_{25}$ predominantly interacting with the RRM2 domain of TDP-43, therefore facilitating TDP-43 LCD-LCD intermolecular contacts which in the absence of GR$_{25}$ were compromised in RRM2-LCD interactions [Fig. 1(e)]. However, if LCD-LCD high-density fluctuations occur in near-interfacial regions, the impact of GR$_{25}$ addition in TDP-43 aging kinetics becomes negligible [as shown in Fig. 2(f)] as GR$_{25}$ primarily colocalizes at the condensate core [Fig. 2(a)]. In agreement with our simulations, arginine-rich

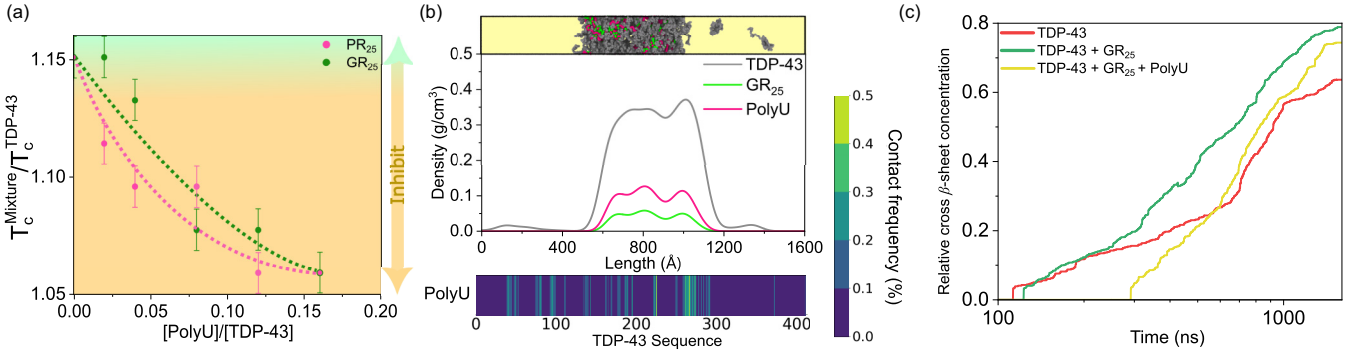

FIG. 3. (a) Variation of the critical solution temperature ($T_c^{\text{System}}/T_c^{\text{TDP-43}}$) as a function of the polyU/TDP-43 molar ratio in TDP-43/GR_{25} and TDP-43/PR_{25} (1:1 molar ratio) mixtures. (b) Top panel: Simulation snapshot and density profile of a TDP-43 + GR_{25} + polyU condensate formed by 100, 100, and 16 molecules of each component respectively (i.e., corresponding to a 0.16 polyU/TDP-43 molar ratio) at 280 K and physiological salt concentration. Density profiles of each species are shown as indicated in the legend. The x axis represents the length of the DC simulation box. Bottom panel: Intermolecular contact frequency of polyU nucleotides with TDP-43 residues in the condensate shown in panel (b) (top). (c) Time-evolution (averaged over five independent trajectories) of the cross-β-sheet concentration (normalized by the maximum number of β-sheets which can be formed in the system) for TDP-43 (red), TDP-43 + GR_{25} (green), and TDP-43 + GR_{25} + polyU (yellow) condensates in coexistence with the diluted phase.

peptides have recently been shown to promote neuronal aging in mice, inhibit ribosome biogenesis, a critical process for protein synthesis, and lead to cellular dysfunction and premature aging [120]. Hence, arginine-rich peptides not only enhance condensate stability but also increase the aging rate of protein condensates into kinetically trapped assemblies. Nevertheless, the growth of cross-β-sheet structures upon nucleation is roughly similar for all the systems studied in agreement with previous computational [100] and experimental work [121].

C. Poly-Uridine RNA reduces the stability of TDP-43/arginine-rich peptide condensates and their propensity to develop β-sheet fibrils

RNA critically regulates the propensity of RNA-binding proteins, such as TDP-43, to undergo phase separation and further maturation [16,101,122–126]. Multiple *in vitro* studies have demonstrated different pathways by which RNAs are capable of modulating protein phase behavior [31,42,104,127–130]. A particularly relevant example is the RNA-driven re-entrant phase behavior of numerous protein condensates in which the length, concentration, and sequence of RNA strands tightly regulate the phase diagram and viscoelastic properties of the condensates [31,85,101,104,131]. In this section, we investigate how polyU single-stranded RNA dictates the stability and aging kinetics of TDP-43/arginine-rich peptide mixtures. We measure the critical solution temperature (through NpT simulations) of TDP-43 condensates—composed of GR_{25} or PR_{25} and TDP-43 at a 1:1 molar ratio—as a function of the polyU concentration using strands of 250 nucleotides [Fig. 3(a)]. Interestingly, our simulations show that the critical temperature monotonically decreases upon polyU addition [Fig. 3(a)]. To better understand this behavior, we also perform DC simulations (see Sec. SV in the SM for details [80]) to unveil the architecture of the condensates [Fig. 3(b), top panel]. We find that RNA predominantly colocalizes at the condensate's core, strongly interacting with GR_{25} (or PR_{25}; Fig. S1 in the SM [80]), driven by attractive electrostatic interactions between R and U. These results are consistent with previous *in silico* work where RNAs of similar length (i.e., from 200 to 400 nucleotides) were found deep within the condensate's core of FUS droplets contributing to strengthening the overall connectivity of the liquid network of the system [101]. By repeating the simulations at a higher temperature ($T = 298$ K), we find that the overall density of the condensate is reduced, although the organization of the condensates remains alike, being polyU and GR_{25} located at the core of the condensate as at $T = 280$ K. Similarly, we explore how variations in the effective NaCl concentration of the system modulates the architecture of condensates. Specifically, we vary the salt concentration from 75 to 300 mM of NaCl (Figs. S6(A) and S6(B) in the SM [80]). While low salt concentration (e.g., 75 mM, Fig. S6A in the SM [80]) promotes higher condensate stability, which correlates with an increase in density within the condensate induced by strongest electrostatic interactions amongst charged residues, higher ionic strength (i.e., 300 mM, Fig. S6B in the SM [80]) destabilizes the condensate leading to a higher concentration of TDP-43 in the dilute phase. These simulations indicate that the critical salt concentration at 280K for this system must be near 300 mM of NaCl given the fact that condensates with protein densities below 0.2 g/cm^3 are usually unstable and eventually dissolve [132].

We now compute the contact frequency distribution of polyU strands with TDP-43 [Fig. 3(b), bottom panel]. While both GR_{25} and PR_{25} predominantly interact with the RRM2 domain—rich in aromatic and negatively charged residues [Fig. 2(b)]—polyU broadly interacts with different segments across the TDP-43 sequence rich in positively charged residues such as arginine and lysine [e.g., scattered from the 45th to the 295th residue; Fig. 3(b)]. However, we note that polyU–TDP-43 contacts are notably weaker than those established by GR_{25} (or PR_{25}) with both TDP-43 and polyU (Fig. S1 in the SM [80]). This suggests that, while RNA interacts with TDP-43, the interaction is much weaker compared to

its interaction with arginine-rich peptides, which is primarily driven by electrostatic nonspecific interactions. Supporting our simulation findings, recent *in vitro* experiments have also shown how arginine-rich peptides (i.e., GR_{20}) establish strong electrostatic interactions between their positively charged side chains and the negatively charged RNA backbone driving condensate formation via complex coacervation [133].

We further perform nonequilibrium DC simulations (e.g., condensates in coexistence with a diluted phase) to characterize the formation of interprotein β-sheet nuclei in TDP-43/GR_{25}/polyU condensates. In Fig. 3(c) we show the time-evolution of cross-β-sheet concentration averaged over 5 independent trajectories with different initial velocities in TDP-43 + GR_{25} + polyU condensates [yellow curve in Fig. 3(c)]. Inclusion of polyU 250-nucleotide strands (at 0.16 polyU/TDP-43 molar ratio) significantly decelerates (i.e., by a factor of $\sim$3) the nucleation time of interprotein β-sheet assemblies compared to pure TDP-43 (red curve) and TDP-43/GR_{25} (green curve) condensates. Interestingly, RNA slows down TDP-43-LCD structural transitions without directly establishing competitive polyU–LARKS interactions as shown in Fig. 3(b) (bottom panel). PolyU outcompetes with TDP-43 to interact with GR_{25}, releasing contacts between GR_{25} and the RRM2 domain of TDP-43 (which contribute to enhancing LCD-LCD interactions driving faster cross-β-sheet formation). Moreover, direct interactions between polyU and the IDR1 in TDP-43, which is adjacent to several rich-aromatic regions prone to undergo β-sheet transitions, are likely contributing to decelerating aging kinetics. Additionally, RNA-RNA electrostatic self-repulsion at moderately high RNA concentration partially reduces the condensate density decreasing the probability of local stacking of TDP-43-LCD driving β-sheet transitions. Overall, the polyU propensity to interact with arginine-rich peptides (Fig. S1 in the SM [80]) and TDP-43 IDR1 [Fig. 3(b)] reduces TDP-43-LCD intermolecular contacts (as it will be further discussed in Sec. II E) and the system kinetics of developing interprotein structural transitions. The addition of single-stranded polyU at high concentrations (i.e., before RNA-driven phase separation inhibition) has also been shown to delay the emergence of cross-β-sheet assemblies in other RNA-binding proteins involved in stress granule formation, such as hnRNPA1 [113] and FUS [74]. Moreover, the importance of heterotypic interactions between proteins and nucleic acids and how these interactions influence the mechanistic pathway and kinetics of amyloid formation have been recently highlighted in Ref. [134]. It has been reported how the presence of RNA influences the transition of hnRNPA1A from a soluble state to amyloid, with the pathways being conducted by the RNA/protein ratio: at lower RNA concentration RNA acts as a facilitator for amyloid formation of hnRNPA1A while at higher RNA concentration condensation is inhibited due to reentrant phase behavior [31,134].

D. HSP70 chaperone and RNA decelerate interprotein β-sheet formation in TDP-43 condensates through alternative yet synergistic mechanisms

The heat-shock protein of 70 kiloDaltons (HSP70) was first identified as part of a protective mechanism triggered by heat stress [135], laying the foundation for understanding its vital role in maintaining protein homeostasis, regulating stress responses, and promoting resilience under adverse conditions [136]. It contains two functional domains: a nucleotide binding domain (NBD) and a substrate binding domain (SBD), which are followed by a C-terminal domain (CTD), as sketched in Fig. 4(a) (please see the protein sequence in Sec. SIII in the SM [80]). The two functional domains are connected by a highly conserved interdomain linker with relevant hydrophobic residues for chaperone function [138]. HSP70 chaperone is one of the most conserved protein sequences throughout different species known in biology [139], and it acts as an essential regulator of protein folding and cellular stress responses. Furthermore, it has been reported to undergo phase separation *in vitro* and cophase separate with different RBPs (such as FUS) preventing them from transitioning abnormally from a liquid state to a solid phase as well as from developing fibrils over time [140,141].

Given its central role in regulating protein phase transitions, this section focuses on exploring its impact on modulating TDP-43 + GR_{25} condensates internal organization and aging kinetics. To that purpose, we first perform DC simulations of a TDP-43/GR_{25}/HSP70 condensate at a molar ratio of 1:1:0.16 [Fig. 4(b)]. We note that the structure of HSP70 [shown in Fig. 4(a)] is maintained across the simulations with the exception of the identified IDRs along the sequence. By performing a density profile of the different species across the condensates, we discover that HSP70 preferentially colocalizes at the condensate's interface, in contrast to TDP-43 and GR_{25} which are homogeneously distributed throughout the condensate. We note that this is an equilibrium configuration of the condensate since all the species were initially randomly distributed across the simulation box and have since reached equilibrium. To reduce the noise of our density profiles computed from DC simulations, we apply a Gaussian smoothing algorithm. The uncertainty of our density profiles computed through DC simulations has been evaluated by bootstrapping block analysis obtaining values below $\sim$7.5% for all the species (please see Sec. SV in the SM for further details on these calculations [80]). To elucidate the impact of ionic strength on the phase behavior of this ternary mixture, we perform simulations at 75 mM and 300 mM NaCl to characterize how variations in salt concentration regulate condensate stability (Figs. S6(C) and S6(D) in the SM [80]). TDP-43 + GR_{25} + HSP70 condensates display increased density at 75 mM NaCl compared to 300 mM, where HSP70 is no longer recruited into the condensate due to the high ionic strength. This is consistent with the notion that HSP70 stabilization within condensates is partly driven by electrostatic contributions from its charged residues, which are enhanced at lower salt concentrations (i.e., 75 mM NaCl). Furthermore, this behavior suggests that HSP70 acts as a client rather than a scaffold, given its lower effective valency—primarily mediated by CTD-LCD heterotypic interactions at 150 mM [Figs. 4(b) and 4(e)]—which are weakened by a moderate increase in the ionic strength (e.g., 300 mM). This observation is also consistent with the behavior of TDP-43 + GR_{25} + polyU condensates (Figs. S6(A) and S6(B) in the SM [80]), where higher salt concentration also reduce

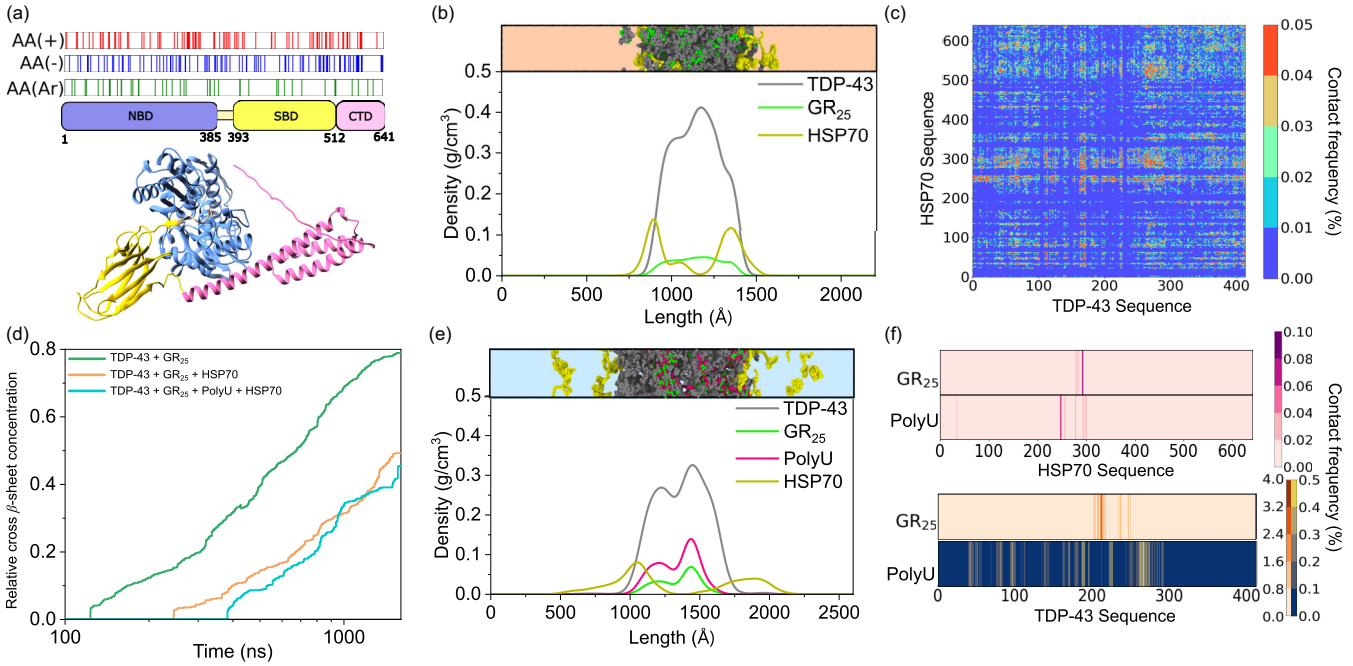

FIG. 4. (a) Scheme of the HSP70 chaperone (1B Homo sapiens NP005337.2.) sequence displaying its different domains: a nucleotide binding domain (NBD) at the N-terminal, a substrate binding domain (SBD), and a C-terminal domain (CTD) [137]. The distribution of the positively and negatively charged amino acids as well as the aromatic residues across the sequence is shown above. (b) Density profile of a DC simulation at $T = 280$ K composed of TDP-43 (gray), HSP70 (khaki), and GR_{25} (green) at 1:0.16:1 molar ratio. The snapshot on top of the panel shows a representative configuration of the DC simulation. (c) Intermolecular contact frequency (in % of contacts per residue) between HSP70 and TDP-43 evaluated in the condensate shown in panel (b). (d) Time-evolution of the cross-β-sheet concentration (averaged for five independent trajectories and normalized by the maximum number of β-sheets which can be formed in the condensate) for different mixtures of TDP-43 condensates as indicated in the legend. (e) Density profile of a DC simulation at 280 K composed of TDP-43 (gray), GR_{25} (green), polyU (pink), and HSP70 (khaki) with a molar stoichiometry of 1:1:0.16:0.16, respectively. Snapshot on top of the panel shows a representative configuration of the DC simulation. (f) Intermolecular contact frequency of polyU and GR_{25} with both HSP70 (top panel) and TDP-43 (bottom panel) in the condensate shown in panel (e).

condensate density and stability. Nevertheless, the fact that polyU remains within the condensate up to 300 mM underscores its higher effective multivalency relative to HSP70, as also supported by the tendency of polyU to localize at the core in contrast to HSP70 which preferentially accumulates at the interface—characteristic of low-valency biomolecules as previously reported in the literature both *in vitro* and *in silico* [142–144].

To uncover the key intermolecular interactions triggering such condensate architecture, we compute the contact frequency map of heterotypic interactions between HSP70 and TDP-43 [Fig. 4(c)]. Among the regions of TDP-43 that interact with HSP70, its LCD is one of the most prominent domains in establishing heterotypic contacts, consistent with previous studies [145] reporting that HSP70 binds to unfolded and predominantly hydrophobic segments of substrate proteins. Additionally, there are two regions of HSP70, within the 250–300 amino acid region—corresponding to a segment across its NBD region—which exhibit high contact frequencies with a significant part of TDP-43 sequence ranging from the 3rd to the 90th residue, and from the 175th to 290th amino acid [Fig. 4(c)]. The nature of the interactions driving such intermolecular contacts are primarily π-π, cation-π, and electrostatic, as these domains are enriched in aromatic and charged residues, including a significant number of glutamic (E) and aspartic (D) acids in TDP-43, lysines (K) and arginines (R) in HSP70, as well as tyrosines (Y) and phenylalanines (F) in segments of both sequences [please see Figs. 2(b) and 4(a)]. Cation-π and π-π interactions are mostly formed between aromatic residues within this region of HSP70 (from the 250th to the 300th residue) and K, R, Y, and F amino acids of TDP-43 within the two aforementioned domains of TDP-43 and its LCD. Nevertheless, the overall frequency of contacts between HSP70 and TDP-43 is lower than that of TPD-43 with GR_{25} and PR_{25} as shown in Fig. 2(b)—being the highest value of heterotypic contacts per residue 0.05% between TDP-43 and HSP70 while almost 4% between both arginine-rich peptides and TDP-43. Thus, the positioning of HSP70 at the interfaces is likely driven by its low effective valency with TDP-43 (and GR_{25}; Fig. S2 in the SM [80]), with only a few specific regions interacting, such as the CTD and LCD of HSP70 and TDP-43, respectively among few others [Fig. 4(c)]. This low effective valency with TDP-43 and GR_{25} may also contribute to reducing the condensate's surface tension with the diluted phase, as previously shown for low-valency colloidal patchy particles forming multilayer condensates [142,143].

We also perform nonequilibrium DC simulations to measure the kinetics of formation of interprotein β-sheet assemblies in TDP-43 + GR_{25} + HSP70 condensates. We run

five independent trajectories with different initial velocities and we measure the concentration of cross-β-sheet structures over time. In Fig. 4(d), we compare the time-evolution of the average relative concentration of cross-β-sheets in condensates formed by TDP-43 and GR_{25} (green curve) and condensates of TDP-43 + GR_{25} + HSP70 (orange curve) with the same molar ratio as that shown in Fig. 4(b). We find that the nucleation time for the formation of the first cross-β-sheet nucleus is significantly decelerated by a factor of 2 when the chaperone is present in the condensate—despite being at a relatively low concentration (TDP-43/HSP70 1:0.16 molar ratio). Such deceleration in aging kinetics is similar to that found in presence of polyU strands of 250 nucleotides at the same molar ratio of 1:0.16 [Fig. 3(c)]. However, while the impact of both HSP70 and polyU on aging kinetics is alike, the molecular mechanism by which they regulate it seems to be radically different. PolyU outcompetes TDP-43 to interact with arginine-rich peptides, releasing contacts among the peptides and the TDP-43 RRM2 domain, and indirectly decreasing LCD-LCD interactions by favoring RRM2-LCD contacts. Moreover, direct interactions between polyU and the IDR1 of TDP-43 (adjacent to several LARKS) contribute to frustrating cross-β-sheet formation as well as RNA-RNA electrostatic self-repulsion which partially reduces condensate density and decreases the probability of TDP-43-LCD stacking. In contrast, HSP70 intervenes through a completely different mechanism in which TDP-43 LCD-LCD interactions seem to be precluded by competing heterotypic contacts with the CTD of HSP70. Moreover, the primarily localization of HSP70 toward the interface may contribute to hinder LCD-LCD stacking (substituted by CTD-LCD interactions) over the interfacial and near-interfacial regions, which as shown in Fig. 2(d), enhance interprotein β-sheet transitions compared to bulk condensate conditions.

Next, we investigate whether the addition of polyU modifies the internal organization of TDP-43 + GR_{25} + HSP70 condensates. We perform DC simulations of a system with the same molar ratio as in Fig. 4(b) but including polyU strands of 250-nucleotides in the same molar ratio as HSP70 (e.g., TDP-43/GR_{25}/HSP70/polyU: 1:1:0.16:0.16). In Fig. 4(e), we show a snapshot of the condensate as well as the density profile across the long axis of the simulation box for each of the different species (see Sec. SV in the SM for further information [80]). Notably, while GR_{25} and polyU predominantly localize within the core of the condensate, HSP70 accumulates at the interface exhibiting low mixing with both RNA and GR_{25}. TDP-43 recruits arginine-rich peptides to the core of the condensate due to their high-affinity binding through the RRM2 region. GR_{25} peptides additionally interact with polyU RNA through electrostatic-driven interactions. Meanwhile, HSP70 predominantly interacts with TDP-43 through CTD-LCD contacts, as well as through interactions between its NBD (mainly from the 250th to the 300th residue) and the NTD/RRM2 domains of TDP-43. The intermolecular contact maps between GR_{25} and polyU with both TDP-43 and HSP70 within the four-component condensate are shown in Fig. 4(f). We consistently find that GR_{25} predominantly contacts with the RRM2 domain of TDP-43 (enriched in aromatic and negatively charged residues) and polyU strands interact with different segments across the TDP-43 sequence enriched in positively charged residues such as arginine and lysine, as shown in Fig. 2(b). Interestingly, the contact frequency maps of GR_{25} and polyU with TDP-43 barely vary in presence of HSP70 (at this concentration) as shown in Figs. 2(b), 3(b), and 4(f). Such contact network distribution is consistent with its known propensity to bind arginine-rich peptides and stabilize condensates in presence of nucleic acids [31]. In contrast to TDP-43, heterotypic contacts between HSP70 and both polyU and GR_{25} are scarce [Fig. 4(f), top panel]. Specifically, GR_{25} interacts with a short segment of the HSP70 NBD region—rich in negatively charged residues (D_{285}, E_{283}, E_{289}, D_{292})—and polyU RNA interacts with different short segments across the sequence containing lysines and arginines (K_{246}, K_{248}, K_{250}, K_{251}, K_{257}, R_{299}, R_{301}). Such small extent of heterotypic contacts with both polyU and GR_{25} further contributes to primarily drive HSP70 localization toward the condensate interface. In that sense, HSP70 can act as a molecular buffer [146], preventing excessive protein compaction and regulating condensate fluidity through specific interactions with hydrophobic protein domains as the TDP-43 LCD. Furthermore, the primary colocalization of HSP70 at the interfaces may play a functional role in protecting the condensate from premature aging initiated in these regions [43,116], as well as contributing to controlling its growth.

We now measure the formation of interprotein β-sheets in TDP-43 + GR_{25} condensates containing both HSP70 and polyU [Fig. 4(d)]. The addition of RNA in TDP-43 + GR_{25} + HSP70 condensates further delays the emergence of cross-β-sheet nuclei. The average nucleation time (from five different independent trajectories) for the onset of cross-β-sheet growth is over three times faster in TDP-43 + GR_{25} condensates (green curve) than in the four-component system (blue curve). This result suggests that HSP70 can further decelerate aging when RNA is present, consistent with its established role as an anti-aggregation chaperone [146]. On the one hand, polyU strands compete with TDP-43 for establishing condensate-stabilizing interactions with GR_{25}, thus indirectly hindering LCD-LCD intermolecular contacts by promoting RRM2-LCD contacts in TDP-43, and polyU-IDR1 TDP-43 interactions which partially destabilize LCD-LCD high-density fluctuations due to RNA-RNA electrostatic self-repulsion. On the other hand, HSP70 at the interface directly competes with TDP-43 to form LCD-LCD intermolecular contacts through heterotypic CTD-LCD interactions. The synergy between the indirect mechanism by which RNA reduces the frequency of TDP-43 LCD-LCD contacts, and the direct interaction of HSP70 with the TDP-43 LCD, as well as the chaperone's localization at the interface, notably decelerates the emergence of cross-β-sheet structures in TDP-43 condensates.

E. TDP-43 LCD intermolecular contact probability dictates the onset of cross-β-sheet nuclei formation

In previous sections, we have shown how the composition of TDP-43 condensates modulates the propensity of TDP-43 LARKS to undergo structural transitions into cross-β-sheet assemblies. While the inclusion of GR_{25} peptides speed up aging kinetics driven by interprotein β-sheet transitions, both polyU and HSP70 decelerate their emergence. To further

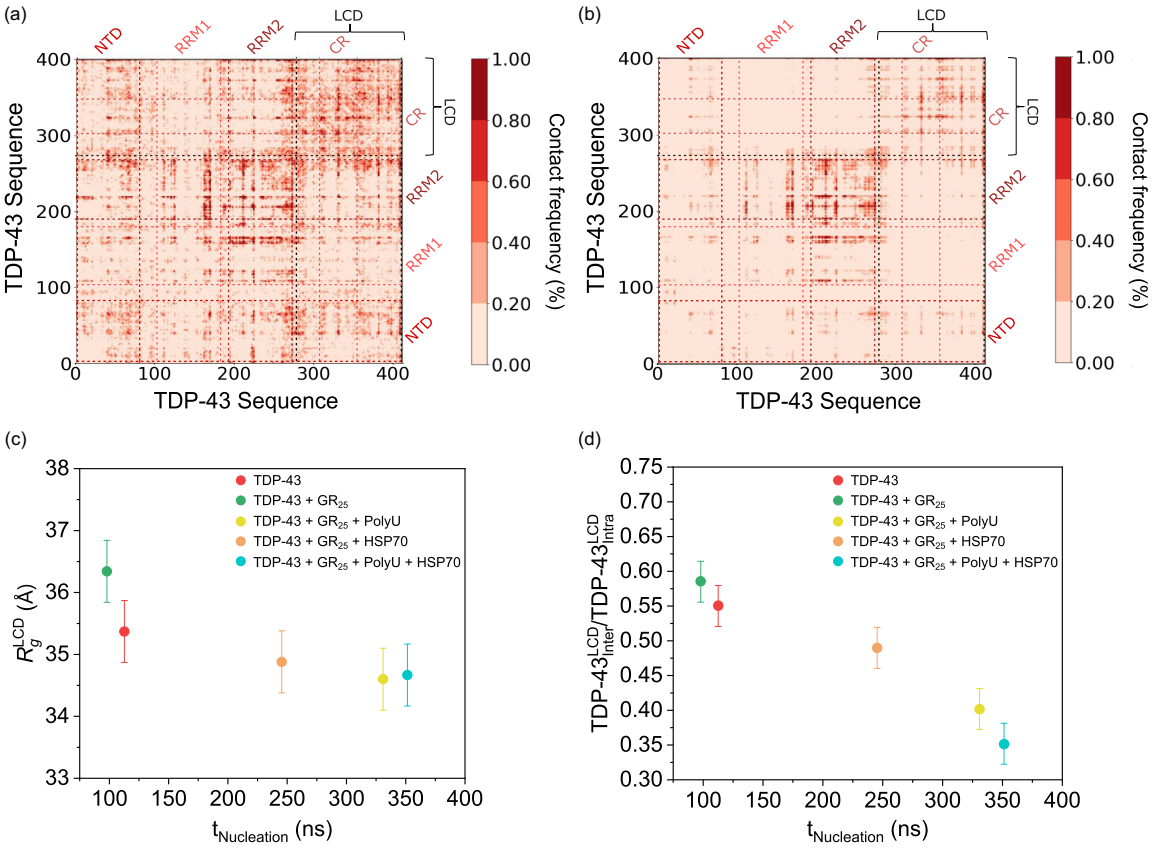

FIG. 5. Map of TDP-43 intermolecular contacts (expressed in percentage per molecule residue) evaluated in TDP-43/GR_{25} condensates at 1:1 molar ratio (a) and TDP-43/GR_{25}/polyU/HSP70 condensates at 1:1:0.16:0.16 molar ratio (b) at $T = 280$ K at their corresponding condensate equilibrium density. Details on these calculations are provided in Sec. SVI of the SM [80]. (c) Radius of gyration (R_g) of the low-complexity domain (LCD) of TDP-43 evaluated for different condensate mixtures as a function of their corresponding average nucleation time of cross-β-sheet clusters. (d) Ratio of intermolecular/intramolecular LCD contacts in TDP-43 for different condensate mixtures vs their average nucleation time of cross-β-sheet formation.

understand the precise mechanism regulating such behavior, we now analyze the frequency of TDP-43 intermolecular contacts in the two most different case scenarios presenting the earliest [Fig. 5(a), TPD-43 + GR_{25}] and latest [Fig. 5(b), TDP-43 + GR_{25} + polyU + HSP70] formation of cross-β-sheet nuclei. We observe that TDP-43 intermolecular contacts (in non-aged liquidlike condensates) decrease almost 50% upon the addition of both HSP-70 and polyU. While the effective reduction of TDP-43 intermolecular contacts is partly due to steric hindrance from additional species within the condensate, we observe that different domains of TDP-43 exhibit varying changes in their contact frequencies. Intermolecular interactions among RRM2 domains of different protein replicas increase over 30% upon polyU and HSP-70 addition. However, the intermolecular contact probability between TDP-43 LCDs—those driving interprotein β-sheet transitions—decrease by almost 30% [Fig. 5(b)]. Such decrease can be mainly ascribed to CTD-LCD interactions between HSP70 and TDP-43 [which outcompete LCD-LCD TDP-43 contacts; Fig. 4(c)], and polyU-IDR1 interactions [Fig. 3(b)]. Overall, while the inclusion of additional species within the condensate contributes to the global reduction of TDP-43 intermolecular contacts, and thus aging, we show here that is not necessarily always the case, since GR_{25} inclusion augments LCD-LCD TDP-43 contact probability, while polyU + HSP70 reduce LCD-LCD interactions and favor RRM2-RRM2 TDP-43 contacts—which do not drive interprotein β-sheet transitions.

Furthermore, since a decisive factor in TDP-43's interprotein β-sheet transitions is how accessible are LCDs to interact with each other, we now evaluate the radius of gyration of the LCD of TDP-43 within condensates with the compositions previously studied. For instance, TDP-43 + GR_{25} condensates display the largest R_g values in TDP-43 LCDs [Fig. 5(c), green circle]. Such more extended conformations are expected to facilitate intermolecular contacts between different LCDs contributing to TDP-43 LCD favorable stacking and promoting interprotein structural transitions. This phenomenon had already been observed in the context of Tau protein [147]. Indeed, TDP-43 + GR_{25} condensates display the shortest timescale before the emergence of cross-β-sheet nuclei of all the studied systems. In contrast, multicomponent condensates—including both polyU RNA and HSP70 in addition to TDP-43 and GR_{25}—promote

TDP-43 LCD conformations which are moderately more compacted [Fig. 5(c), cyan circle] and present the slowest nucleation time of cross-β-sheet formation [Fig. 4(d)]. Hence, our simulations suggest a correlation between the LCD structural level of compaction—modulated by the presence of additional species—and the kinetics of cross-β-sheet formation [Fig. 5(c)]. To further understand these differences in R_g among the different condensates, we also evaluate the ratio of inter- versus intramolecular LCD contacts [Fig. 5(d)]. Higher ratios of intermolecular/intramolecular contacts are expected to favor LCD-LCD interactions triggering cross-β-sheet transitions. Figure 5(d) reveals a strong correlation between higher inter/intra molecular contacts of the LCD and faster nucleation times of cross-β-sheet assemblies. This also indicates how larger R_g values of the LCD (i.e., more extended conformations) enable higher intermolecular contact frequencies, which in turn lead to faster aging kinetics. Therefore, the way in which additional components to the scaffold protein—such as nucleic acids, peptides, or other proteins—regulate the accessibility of LARKS-containing LCDs determine the propensity to undergo cross-β-sheet transitions and progressive kinetic arrest over time.

III. CONCLUSIONS

In this work, we investigate the impact of various biomolecules—such as arginine-rich peptides, RNA, and the HSP70 chaperone—on the stability, internal organization, and aging kinetics of condensates formed by TDP-43, a key RNA-binding protein that drives stress granule formation. We perform Molecular Dynamics simulations of the Mpipi-Recharged model [75], a coarse-grained residue resolution force field particularly designed for an accurate description of charge effects in biomolecular condensates, while maintaining the excellent predictions for low-complexity domains and multidomain proteins of its predecessor Mpipi [60]. We find that while the model overestimates the experimental protein saturation concentration values of TDP-43 to undergo phase separation [20,82,83] [Fig. 1(c)], it closely reproduces *in vitro* experimental values of a TDP-43 mutant radius of gyration under diluted conditions [81], as well as atomistic modeling predictions [13] [Fig. 1(b)]. Furthermore, we benchmark the Mpipi-Recharged predictions of TDP-43 condensate stability as a function of different dipeptide repeats, such as GP_{25}, GR_{25}, and PR_{25} [Fig. 2(a)] against *in vitro* experiments [16,18,27]. Our model reproduces the reentrant phase behavior of TDP-43 condensates upon the addition of GR_{25} and PR_{25}, capturing the peptide/protein molar ratio of condensate maximum stability [16,18,27], and the monotonically decreasing stability after the inclusion of GP_{25} [16]. Our simulations show that the main contacts enabling TDP-43 phase separation are interactions between the RRM2-RRM2, RRM1-RRM2, and LCD-LCD regions, mainly involving aromatic and charged residues that contribute to the condensate's intermolecular connectivity. This is in agreement with previous experimental findings [96] [Fig. 1(e)]. However, in the presence of arginine-rich peptides, and at the stoichiometry that maximizes the stability of the condensate (i.e., 1:1 molar ratio), the heterotypic contacts enhancing condensate stability are mostly electrostatic and cation-π interactions between GR_{25} (or PR_{25}) and the RRM2 domain of TDP-43 which is rich in aromatic and negatively charged residues [Fig. 2(b)].

We perform nonequilibrium simulations using our aging algorithm [53,113] to investigate the formation of cross-β-sheet clusters in TDP-43 condensates over time. Interestingly, we discover that both pure TDP-43 and TDP-43 + GR_{25} condensates exhibit faster nucleation of cross-β-sheet structures in condensates simulated in coexistence with the protein diluted phase than in condensate bulk conditions [Fig. 2(d)]. These results suggest that interprotein structural β-sheet transitions might be favored at interfacial or near-interfacial regions in TDP-43 condensates as previously found for FUS [43,53], α-synuclein [115], and hnRNPA1 [116] condensates. Moreover, we find that the recruitment of arginine-rich peptides such as GR_{25} also accelerates the emergence of interprotein β-sheet clusters as compared to pure TDP-43 systems [Fig. 2(f)]. Hence, in addition to increasing their cohesion up to moderately high molar ratios, arginine-rich peptides also enhance their transition into aged kinetically trapped assemblies. The strong interaction that both GR_{25} and PR_{25} establish with the TDP-43 RRM2 region [Fig. 2(b)] partially releases RRM2-LCD contacts, thus indirectly increasing the frequency of LCD-LCD intermolecular interactions which trigger cross-β-sheet transitions.

We also determine the stability limits of TDP-43 + GR_{25} condensates as a function of the concentration of polyU RNA. The addition of polyU moderately decreases the critical solution temperature of the condensates [Fig. 3(a)]. PolyU predominantly colocalizes at the condensate core strongly interacting with GR_{25} (Fig. 3(b) and Fig. S1 in the SM [80]) driven by attractive nonspecific electrostatic interactions—in agreement with previous experimental and computational findings for other RNA-binding proteins including FUS [101,133]. The binding affinity of polyU is lower with TDP-43 than with GR_{25}, only establishing significant interactions with its IDR1 domain and other different short segments along the sequence which are enriched in positively charged residues [Fig. 3(b)]. Notably, the inclusion of polyU decelerates by twofold the nucleation time of cross-β-sheet assemblies compared to TDP-43 + GR_{25} condensates [Fig. 3(c)], outcompeting with TDP-43 to interact with GR_{25} (Fig. S1 in the SM [80]) and overall reducing TDP-43 LCD intermolecular contacts. While polyU strands do not establish direct interactions with TDP-43 LARKS [Fig. 3(b)], they compete with TDP-43 to interact with GR_{25}, releasing contacts between GR_{25} and the RRM2 domain of TDP-43, which consequently enable RRM2-LCD interactions hindering cross-β-sheet transitions. Moreover, direct interactions between polyU and the IDR1 of TDP-43, which has several adjacent LARKS, contribute to decelerating aging kinetics according to our model. Additionally, the electrostatic self-repulsion among polyU strands at a moderately high concentration locally reduces the condensate density, thus hindering the frequency of TDP-43-LCD stacking promoting β-sheet transitions.

Furthermore, we introduce the chaperone HSP70 into TDP-43 + GR_{25} condensates. HSP70 primarily concentrates at the condensate's interface at physiological and low salt concentrations (Fig. 4(b) and Figs. S6(C) and S6(D) in the SM [80]) establishing a low number of contacts with GR_{25}

and several domains of TDP-43 sequence (i.e., NTD, RMM2 or LCD). The interactions between TDP-43 and HSP70 are mediated primarily by π-π, cation-π, and electrostatic contacts, establishing the (HSP70) CTD and the (TDP-43) LCD the most relevant intermolecular interactions between both species [Fig. 4(c)]. Such observation is consistent with previous work [145] suggesting hydrophobiclike interactions to be critical for chaperones, in particular HSP70, in preventing protein aberrant aggregation. HSP70 decelerates the emergence of cross-β-sheet clusters by a factor of 2 [Fig. 4(d)], which is similar to the nucleation rate slow down induced through polyU inclusion. However, the mechanism by which HSP70 reduces interprotein β-sheet transitions is through a direct competition of CTD-LCD contacts between HSP70 and TDP-43 versus LCD-LCD interactions among TDP-43 proteins. The maximum deceleration in the formation of cross-β-sheet nuclei is achieved when both HSP70 and polyU are recruited within TDP-43 + GR_{25} condensates [Fig. 4(d)]. The synergy between the indirect mechanism by which RNA reduces the contact probability of TDP-43 LCD-LCD contacts, and the direct competition of HSP70 for TDP-43 LCD-LCD interactions delays the emergence of cross-β-sheet structures by a factor of 3 with respect to TDP-43/GR_{25} mixtures, which are those exhibiting fastest aging kinetics. We note that the deceleration through polyU and HSP70 insertion can depend significantly on the stoichiometry of the mixture, as previously shown for FUS and hnRNPA1 + polyU condensates [113]. Remarkably, even at low stoichiometric ratios of both polyU and HSP70 as studied here, their impact on aging kinetics seems to be substantial.

Finally, we determine that the number of intermolecular contacts that TDP-43 homotypically establishes in the presence of GR_{25} [Fig. 5(a)] doubles the number upon addition of both polyU and HSP70 to TDP-43 + GR_{25} condensates [Fig. 5(b)], despite the latter species being present at a much lower molar ratio (six times less) than TDP-43 and GR_{25}. While this reduction is in part due to steric hindrance from additional species within the condensate, we observe that intermolecular interactions between TDP-43 RRM2 domains increase in presence of polyU and HSP70 with respect to TDP-43 + GR_{25} condensates—the system exhibiting fastest aging kinetics. However, a 30% reduction in LCD-LCD contacts is achieved upon inclusion of polyU and HSP70. Furthermore, our simulations show a correlation between aging kinetics and the ratio of intermolecular/intramolecular contacts of TDP-43 LCDs, which in turn also correlates with its degree of compaction evaluated through its radius of gyration [Figs. 5(c) and 5(d)]. Condensate mixtures exhibiting faster nucleation times of cross-β-sheet transitions are scaffolded by TDP-43 proteins which in average possess more extended LCD conformations, and hence, higher probability of establishing LCD-LCD intermolecular contacts. The inclusion of different biomolecules to the scaffold protein—such as nucleic acids, peptides, or other proteins—regulates the accessibility of LCDs containing LARKS and determines the propensity to undergo cross-β-sheet transitions and progressive kinetic arrest. Altogether, our simulations provide molecular-level insights into the key interactions, mechanisms, and specific factors that might modulate the condensate phase behavior of RNA-binding proteins, such as TDP-43, implicated in neurodegenerative diseases. Elucidating the microscopic pathways underlying aberrant liquid-to-solid transitions of condensates is crucial for developing potential therapeutic strategies to control condensate dynamics, given their broad implications in health and disease.

ACKNOWLEDGMENTS

A.F. acknowledges funding from the Ramon y Cajal fellowship (Grant No. RYC2021-030937-I) and Spanish National (Grant No. PID2022-136919NA-C33). I.S.-B. acknowledges funding from Derek Brewer scholarship of Emmanuel College and EPSRC Doctoral Training Programme studentship, Grant No. EP/T517847/1, Ramon y Cajal fellowship (awarded to J.R.E.), as well as the UKRI EPSRC under the U.K. Government's guarantee scheme (Grant No. EP/Z002028/1), following successful evaluation by the ERC (Consolidator Grant awarded to R.C.G.) under the European Union's Horizon Europe research and innovation programme. A.R. acknowledges funding from PID2023-147156NB-I00 of the Spanish Ministry for Science, Innovation and Universities. R.C.-G. acknowledges funding from the European Research Council (ERC) under the European Union Horizon 2020 research and innovation programme (Grant Agreement No. 803326). A.R.T. acknowledges funding from the European Union Horizon 2020 research and innovation programme (Grant Agreement No. 803326 to R.C.-G.). J.R.E. acknowledges funding from Emmanuel College, the University of Cambridge, the Ramon y Cajal fellowship (Grant No. RYC2021-030937-I), and the Spanish scientific plan and committee for Research Reference No. PID2022-136919NA-C33 and the European Research Council (ERC) under the European Unions Horizon Europe research and innovation program (Grant Agreement No. 101160499). E.P. acknowledges funding from European Social Fund Plus and Project No. PID2022-136919NA-C33 from the the Spanish MICIU. M.M.C. acknowledges funding from the Ministerio de Ciencia e Innovación (Grant No. PID2022-136919NB-C32). This work has been performed using resources provided by the Cambridge Tier-2 system operated by the University of Cambridge Research Computing Service [163] funded by EPSRC Tier-2 capital Grant No. EP/P020259/1-CS170. This work has also been performed using resources provided by Archer2 [164] funded by EPSRC Tier-2 capital Grant No. EP/P020259/e829. The authors also thankfully acknowledge RES computational resources provided by Mare Nostrum 5 through the activity 2024-3-0001 and 2025-1-0009. The authors gratefully acknowledge the Universidad Politecnica de Madrid [165] for providing computing resources on Magerit Supercomputer [166].

DATA AVAILABILITY

The data that support the findings of this article are openly available [167].

[1] Y. M. Ayala, S. Pantano, A. D'Ambrogio, E. Buratti, A. Brindisi, C. Marchetti, M. Romano, and F. E. Baralle, Human, drosophila, and C. elegans TDP43: Nucleic acid binding properties and splicing regulatory function, J. Mol. Biol. **348**, 575 (2005).

[2] A. Wang, A. E. Conicella, H. B. Schmidt, E. W. Martin, S. N. Rhoads, A. N. Reeb, A. Nourse, D. Ramirez Montero, V. H. Ryan, R. Rohatgi *et al.*, A single n-terminal phosphomimic disrupts TDP-43 polymerization, phase separation, and RNA splicing, EMBO J. **37**, e97452 (2018).

[3] M. J. Strong, The evidence for altered RNA metabolism in amyotrophic lateral sclerosis (ALS), J. Neurol. Sci. **288**, 1 (2010).

[4] F. Bright, G. Chan, A. van Hummel, L. M. Ittner, and Y. D. Ke, TDP-43 and inflammation: Implications for amyotrophic lateral sclerosis and frontotemporal dementia, Int. J. Mol. Sci. **22**, 7781 (2021).

[5] W.-C. Chiang, M.-H. Lee, T.-C. Chen, and J.-r. Huang, Interactions between the intrinsically disordered regions of hnRNP-A2 and TDP-43 accelerate TDP-43's conformational transition, Int. J. Mol. Sci. **21**, 5930 (2020).

[6] S. Da Cruz and D. W. Cleveland, Understanding the role of TDP-43 and FUS/TLS in ALS and beyond, Current Opin. Neurobiol. **21**, 904 (2011).

[7] P. Masrori and P. Van Damme, Amyotrophic lateral sclerosis: A clinical review, Eur. J. Neurology **27**, 1918 (2020).

[8] P. P. Gopal, J. J. Nirschl, E. Klinman, and E. L. Holzbaur, Amyotrophic lateral sclerosis-linked mutations increase the viscosity of liquid-like TDP-43 RNP granules in neurons, Proc. Natl. Acad. Sci. USA **114**, E2466 (2017).

[9] I. R. Mackenzie, R. Rademakers, and M. Neumann, TDP-43 and FUS in amyotrophic lateral sclerosis and frontotemporal dementia, Lancet Neurol. **9**, 995 (2010).

[10] M. Kato, T. W. Han, S. Xie, K. Shi, X. Du, L. C. Wu, H. Mirzaei, E. J. Goldsmith, J. Longgood, J. Pei *et al.*, Cell-free formation of rna granules: Low complexity sequence domains form dynamic fibers within hydrogels, Cell **149**, 753 (2012).

[11] A. F. Harrison and J. Shorter, RNA-binding proteins with prion-like domains in health and disease, Biochem. J. **474**, 1417 (2017).

[12] A. Patel, H. O. Lee, L. Jawerth, S. Maharana, M. Jahnel, M. Y. Hein, S. Stoynov, J. Mahamid, S. Saha, T. M. Franzmann *et al.*, A liquid-to-solid phase transition of the ALS protein FUS accelerated by disease mutation, Cell **162**, 1066 (2015).

[13] P. Mohanty, A. Rizuan, Y. C. Kim, N. L. Fawzi, and J. Mittal, A complex network of interdomain interactions underlies the conformational ensemble of monomeric TDP-43 and modulates its phase behavior, Protein Sci. **33**, e4891 (2024).

[14] S. S. Keating, A. T. Bademosi, R. San Gil, and A. K. Walker, Aggregation-prone TDP-43 sequesters and drives pathological transitions of free nuclear TDP-43, Cell. Mol. Life Sci. **80**, 95 (2023).

[15] E. L. Guenther, Q. Cao, H. Trinh, J. Lu, M. R. Sawaya, D. Cascio, D. R. Boyer, J. A. Rodriguez, M. P. Hughes, and D. S. Eisenberg, Atomic structures of TDP-43 LCD segments and insights into reversible or pathogenic aggregation, Nat. Struct. Mol. Biol. **25**, 463 (2018).

[16] S. Hutten, S. Usluer, B. Bourgeois, F. Simonetti, H. M. Odeh, C. M. Fare, M. Czuppa, M. Hruska-Plochan, M. Hofweber, M. Polymenidou *et al.*, Nuclear import receptors directly bind to arginine-rich dipeptide repeat proteins and suppress their pathological interactions, Cell Rep. **33**, 108538 (2020).

[17] K. Hou, P. Ge, M. R. Sawaya, L. Lutter, J. L. Dolinsky, Y. Yang, Y. X. Jiang, D. R. Boyer, X. Cheng, J. Pi *et al.*, How short peptides disassemble tau fibrils in Alzheimer's disease, Nature (London) **644**, 1020 (2025).

[18] K.-H. Lee, P. Zhang, H. J. Kim, D. M. Mitrea, M. Sarkar, B. D. Freibaum, J. Cika, M. Coughlin, J. Messing, A. Molliex *et al.*, C9ORF72 dipeptide repeats impair the assembly, dynamics, and function of membrane-less organelles, Cell **167**, 774 (2016).

[19] B. D. Freibaum and J. P. Taylor, The role of dipeptide repeats in C9orf72-related ALS-FTD, Front. Mol. Neurosci. **10**, 35 (2017).

[20] L. McGurk, E. Gomes, L. Guo, J. Mojsilovic-Petrovic, V. Tran, R. G. Kalb, J. Shorter, and N. M. Bonini, Poly (ADP-ribose) prevents pathological phase separation of TDP-43 by promoting liquid demixing and stress granule localization, Mol. Cell **71**, 703 (2018).

[21] M. Pérez-Berlanga, V. I. Wiersma, A. Zbinden, L. De Vos, U. Wagner, C. Foglieni, I. Mallona, K. M. Betz, A. Cléry, J. Weber *et al.*, Loss of TDP-43 oligomerization or RNA binding elicits distinct aggregation patterns, EMBO J. **42**, e111719 (2023).

[22] M. Polymenidou, The RNA face of phase separation, Science **360**, 859 (2018).

[23] I. Kwon, S. Xiang, M. Kato, L. Wu, P. Theodoropoulos, T. Wang, J. Kim, J. Yun, Y. Xie, and S. L. McKnight, Poly-dipeptides encoded by the C9orf72 repeats bind nucleoli, impede RNA biogenesis, and kill cells, Science **345**, 1139 (2014).

[24] K. Kanekura, T. Yagi, A. J. Cammack, J. Mahadevan, M. Kuroda, M. B. Harms, T. M. Miller, and F. Urano, Poly-dipeptides encoded by the C9ORF72 repeats block global protein translation, Hum. Mol. Genet. **25**, 1803 (2016).

[25] S. Boeynaems, E. Bogaert, D. Kovacs, A. Konijnenberg, E. Timmerman, A. Volkov, M. Guharoy, M. De Decker, T. Jaspers, V. H. Ryan *et al.*, Phase separation of C9orf72 dipeptide repeats perturbs stress granule dynamics, Mol. Cell **65**, 1044 (2017).

[26] M. Yamakawa, D. Ito, T. Honda, K.-i. Kubo, M. Noda, K. Nakajima, and N. Suzuki, Characterization of the dipeptide repeat protein in the molecular pathogenesis of C9FTD/ALS, Hum. Mol. Genet. **24**, 1630 (2015).

[27] R. Balendra and A. M. Isaacs, C9orf72-mediated ALS and FTD: Multiple pathways to disease, Nat. Rev. Neurol. **14**, 544 (2018).

[28] M. DeJesus-Hernandez, I. R. Mackenzie, B. F. Boeve, A. L. Boxer, M. Baker, N. J. Rutherford, A. M. Nicholson, N. A. Finch, H. Flynn, J. Adamson *et al.*, Expanded GGGGCC hexanucleotide repeat in noncoding region of C9ORF72 causes chromosome 9p-linked FTD and ALS, Neuron **72**, 245 (2011).

[29] K. Mori, S.-M. Weng, T. Arzberger, S. May, K. Rentzsch, E. Kremmer, B. Schmid, H. A. Kretzschmar, M. Cruts, C. Van Broeckhoven *et al.*, The C9ORF72 GGGGCC repeat is translated into aggregating dipeptide-repeat proteins in FTLD/ALS, Science **339**, 1335 (2013).

[30] K. Mori, T. Arzberger, F. A. Grässer, I. Gijselinck, S. May, K. Rentzsch, S.-M. Weng, M. H. Schludi, J. van der Zee,

M. Cruts *et al.*, Bidirectional transcripts of the expanded C9orf72 hexanucleotide repeat are translated into aggregating dipeptide repeat proteins, Acta Neuropathol. **126**, 881 (2013).

[31] S. Maharana, J. Wang, D. K. Papadopoulos, D. Richter, A. Pozniakovsky, I. Poser, M. Bickle, S. Rizk, J. Guillén-Boixet, T. M. Franzmann *et al.*, RNA Buffers the phase separation behavior of prion-like RNA binding proteins, Science **360**, 918 (2018).

[32] D. M. Mitrea and R. W. Kriwacki, Phase separation in biology: Functional organization of a higher order, Cell Commun. Signal. **14**, 1 (2016).

[33] J. A. Bard and D. A. Drummond, Chaperone regulation of biomolecular condensates, Front. Biophys. **2**, 1342506 (2024).

[34] D. Mateju, T. M. Franzmann, A. Patel, A. Kopach, E. E. Boczek, S. Maharana, H. O. Lee, S. Carra, A. A. Hyman, and S. Alberti, An aberrant phase transition of stress granules triggered by misfolded protein and prevented by chaperone function, EMBO J. **36**, 1669 (2017).

[35] R. Lang, R. E. Hodgson, and T. A. Shelkovnikova, TDP-43 in nuclear condensates: Where, how, and why, Biochem. Soc. Trans. **52**, 1809 (2024).

[36] L. Jawerth, E. Fischer-Friedrich, S. Saha, J. Wang, T. Franzmann, X. Zhang, J. Sachweh, M. Ruer, M. Ijavi, S. Saha *et al.*, Protein condensates as aging Maxwell fluids, Science **370**, 1317 (2020).

[37] S. Elbaum-Garfinkle, Y. Kim, K. Szczepaniak, C. C.-H. Chen, C. R. Eckmann, S. Myong, and C. P. Brangwynne, The disordered P granule protein LAF-1 drives phase separation into droplets with tunable viscosity and dynamics, Proc. Natl. Acad. Sci. USA **112**, 7189 (2015).

[38] M.-T. Wei, S. Elbaum-Garfinkle, A. S. Holehouse, C. C.-H. Chen, M. Feric, C. B. Arnold, R. D. Priestley, R. V. Pappu, and C. P. Brangwynne, Phase behaviour of disordered proteins underlying low density and high permeability of liquid organelles, Nat. Chem. **9**, 1118 (2017).

[39] H. Zhang, S. Elbaum-Garfinkle, E. M. Langdon, N. Taylor, P. Occhipinti, A. A. Bridges, C. P. Brangwynne, and A. S. Gladfelter, RNA controls polyQ protein phase transitions, Mol. Cell **60**, 220 (2015).

[40] D. Michieletto and M. Marenda, Rheology and viscoelasticity of proteins and nucleic acids condensates, JACS Au **2**, 1506 (2022).

[41] A. Molliex, J. Temirov, J. Lee, M. Coughlin, A. P. Kanagaraj, H. J. Kim, T. Mittag, and J. P. Taylor, Phase separation by low complexity domains promotes stress granule assembly and drives pathological fibrillization, Cell **163**, 123 (2015).

[42] L. Guo and J. Shorter, It's raining liquids: RNA tunes viscoelasticity and dynamics of membraneless organelles, Mol. Cell **60**, 189 (2015).

[43] Y. Shen, A. Chen, W. Wang, Y. Shen, F. S. Ruggeri, S. Aime, Z. Wang, S. Qamar, J. R. Espinosa, A. Garaizar *et al.*, The liquid-to-solid transition of FUS is promoted by the condensate surface, Proc. Natl. Acad. Sci. USA **120**, e2301366120 (2023).

[44] I. Alshareedah, W. M. Borcherds, S. R. Cohen, A. Singh, A. E. Posey, M. Farag, A. Bremer, G. W. Strout, D. T. Tomares, R. V. Pappu *et al.*, Sequence-specific interactions determine viscoelasticity and ageing dynamics of protein condensates, Nat. Phys. **20**, 1482 (2024).

[45] A. Jain and R. D. Vale, RNA phase transitions in repeat expansion disorders, Nature (London) **546**, 243 (2017).

[46] S. Ray, N. Singh, R. Kumar, K. Patel, S. Pandey, D. Datta, J. Mahato, R. Panigrahi, A. Navalkar, S. Mehra *et al.*, α-Synuclein aggregation nucleates through liquid–liquid phase separation, Nat. Chem. **12**, 705 (2020).

[47] S. F. Banani, H. O. Lee, A. A. Hyman, and M. K. Rosen, Biomolecular condensates: Organizers of cellular biochemistry, Nat. Rev. Mol. Cell Biol. **18**, 285 (2017).

[48] S. Ambadipudi, J. Biernat, D. Riedel, E. Mandelkow, and M. Zweckstetter, Liquid–liquid phase separation of the microtubule-binding repeats of the Alzheimer-related protein tau, Nat. Commun. **8**, 275 (2017).

[49] S. Jang, Z. Xuan, R. C. Lagoy, L. M. Jawerth, I. J. Gonzalez, M. Singh, S. Prashad, H. S. Kim, A. Patel, D. R. Albrecht *et al.*, Phosphofructokinase relocalizes into subcellular compartments with liquid-like properties *in vivo*, Biophys. J. **120**, 1170 (2021).

[50] S. J. Nair, L. Yang, D. Meluzzi, S. Oh, F. Yang, M. J. Friedman, S. Wang, T. Suter, I. Alshareedah, A. Gamliel *et al.*, Phase separation of ligand-activated enhancers licenses cooperative chromosomal enhancer assembly, Nat. Struct. Mol. Biol. **26**, 193 (2019).

[51] S. Ray and A. K. Buell, Emerging experimental methods to study the thermodynamics of biomolecular condensate formation, J. Chem. Phys. **160**, 091001 (2024).

[52] Y. Shen, F. S. Ruggeri, D. Vigolo, A. Kamada, S. Qamar, A. Levin, C. Iserman, S. Alberti, P. S. George-Hyslop, and T. P. Knowles, Biomolecular condensates undergo a generic shear-mediated liquid-to-solid transition, Nat. Nanotechnol. **15**, 841 (2020).

[53] A. Garaizar, J. R. Espinosa, J. A. Joseph, G. Krainer, Y. Shen, T. P. Knowles, and R. Collepardo-Guevara, Aging can transform single-component protein condensates into multiphase architectures, Proc. Natl. Acad. Sci. USA **119**, e2119800119 (2022).

[54] B. S. Schuster, G. L. Dignon, W. S. Tang, F. M. Kelley, A. K. Ranganath, C. N. Jahnke, A. G. Simpkins, R. M. Regy, D. A. Hammer, M. C. Good *et al.*, Identifying sequence perturbations to an intrinsically disordered protein that determine its phase-separation behavior, Proc. Natl. Acad. Sci. USA **117**, 11421 (2020).

[55] I. Ivani, P. D. Dans, A. Noy, A. Pérez, I. Faustino, A. Hospital, J. Walther, P. Andrio, R. Goñi, A. Balaceanu *et al.*, Parmbsc1: A refined force field for DNA simulations, Nat. Methods **13**, 55 (2016).

[56] M. Paloni, R. Bailly, L. Ciandrini, and A. Barducci, Unraveling molecular interactions in liquid–liquid phase separation of disordered proteins by atomistic simulations, J. Phys. Chem. B **124**, 9009 (2020).

[57] Z. Brotzakis and P. G. Bolhuis, Unbiased atomistic insight into the mechanisms and solvent role for globular protein dimer dissociation, J. Phys. Chem. B **123**, 1883 (2019).

[58] S. Torrino, W. M. Oldham, A. R. Tejedor, I. S. Burgos, L. Nasr, N. Rachedi, K. Fraissard, C. Chauvet, C. Sbai, B. P. O'Hara *et al.*, Mechano-dependent sorbitol accumulation supports biomolecular condensate, Cell **188**, 447 (2025).

[59] G. L. Dignon, W. Zheng, Y. C. Kim, R. B. Best, and J. Mittal, Sequence determinants of protein phase behavior from

a coarse-grained model, PLoS Comput. Biol. **14**, e1005941 (2018).

[60] J. A. Joseph, A. Reinhardt, A. Aguirre, P. Y. Chew, K. O. Russell, J. R. Espinosa, A. Garaizar, and R. Collepardo-Guevara, Physics-driven coarse-grained model for biomolecular phase separation with near-quantitative accuracy, Nat. Comput. Sci. **1**, 732 (2021).

[61] G. Tesei and K. Lindorff-Larsen, Improved predictions of phase behavior of intrinsically disordered proteins by tuning the interaction range, Open Res. Europe **2**, 94 (2023).

[62] S. Das, Y.-H. Lin, R. M. Vernon, J. D. Forman-Kay, and H. S. Chan, Comparative roles of charge, π, and hydrophobic interactions in sequence-dependent phase separation of intrinsically disordered proteins, Proc. Natl. Acad. Sci. USA **117**, 28795 (2020).

[63] J. M. Walker, H.-X. Zhou, J.-H. Spille, and P. R. Banerjee, *Phase-Separated Biomolecular Condensates—Methods and Protocols*, Methods in Molecular Biology (Humana Press, Totowa, NJ, 2023)

[64] A. R. Tejedor, R. Collepardo-Guevara, J. Ramirez, and J. R. Espinosa, Time-dependent material properties of aging biomolecular condensates from different viscoelasticity measurements in molecular dynamics simulations, J. Phys. Chem. B **127**, 4441 (2023).

[65] K. Sarthak, D. Winogradoff, Y. Ge, S. Myong, and A. Aksimentiev, Benchmarking molecular dynamics force fields for all-atom simulations of biological condensates, J. Chem. Theory Comput. **19**, 3721 (2023).

[66] J. R. Espinosa, J. A. Joseph, I. Sanchez-Burgos, A. Garaizar, D. Frenkel, and R. Collepardo-Guevara, Liquid network connectivity regulates the stability and composition of biomolecular condensates with many components, Proc. Natl. Acad. Sci. USA **117**, 13238 (2020).

[67] W. M. Jacobs and D. Frenkel, Phase transitions in biological systems with many components, Biophys. J. **112**, 683 (2017).

[68] C. Mathieu, R. V. Pappu, and J. P. Taylor, Beyond aggregation: Pathological phase transitions in neurodegenerative disease, Science **370**, 56 (2020).

[69] Y. Zhang, Y. Wang, Y. Liu, G. Wei, F. Ding, and Y. Sun, Molecular insights into the misfolding and dimerization dynamics of the full-length α-synuclein from atomistic discrete molecular dynamics simulations, ACS Chem. Neurosci. **13**, 3126 (2022).

[70] G. F. Martins and N. Galamba, Wild-type α-synuclein structure and aggregation: A comprehensive coarse-grained and all-atom molecular dynamics study, J. Chem. Inf. Model. **64**, 6115 (2024).

[71] Y. Chebaro, N. Mousseau, and P. Derreumaux, Structures and thermodynamics of alzheimer's amyloid-β Aβ(16-35) monomer and dimer by replica exchange molecular dynamics simulations: Implication for full-length Aβ fibrillation, J. Phys. Chem. B **113**, 7668 (2009).

[72] B. Szała-Mendyk, T. M. Phan, P. Mohanty, and J. Mittal, Challenges in studying the liquid-to-solid phase transitions of proteins using computer simulations, Curr. Opin. Chem. Biol. **75**, 102333 (2023).

[73] A. Garaizar, J. R. Espinosa, J. A. Joseph, and R. Collepardo-Guevara, Kinetic interplay between droplet maturation and coalescence modulates shape of aged protein condensates, Sci. Rep. **12**, 4390 (2022).

[74] S. Blazquez, I. Sanchez-Burgos, J. Ramirez, T. Higginbotham, M. M. Conde, R. Collepardo-Guevara, A. R. Tejedor, and J. R. Espinosa, Location and concentration of aromatic-rich segments dictates the percolating intermolecular network and viscoelastic properties of aging condensates, Adv. Sci. **10**, 2207742 (2023).

[75] A. R. Tejedor, A. Aguirre Gonzalez, M. J. Maristany, P. Y. Chew, K. Russell, J. Ramirez, J. R. Espinosa, and R. Collepardo-Guevara, Chemically informed coarse-graining of electrostatic forces in charge-rich biomolecular condensates, ACS Cent. Sci. **11**, 302 (2025).

[76] A. Feito, I. Sanchez-Burgos, I. Tejero, E. Sanz, A. Rey, R. Collepardo-Guevara, A. R. Tejedor, and J. R. Espinosa, Benchmarking residue-resolution protein coarse-grained models for simulations of biomolecular condensates, PLoS Comput. Biol. **21**, e1012737 (2025).

[77] A. Feito, I. Sanchez-Burgos, A. Rey, R. Collepardo-Guevara, J. R. Espinosa, and A. R. Tejedor, Capturing single-molecule properties does not ensure accurate prediction of biomolecular phase diagrams, Mol. Phys. **122** e2425757 (2024).

[78] F. Cao, S. von Bülow, G. Tesei, and K. Lindorff-Larsen, A coarse-grained model for disordered and multi-domain proteins, Protein Sci. **33**, e5172 (2024).

[79] X. Wang, S. Ramírez-Hinestrosa, J. Dobnikar, and D. Frenkel, The Lennard-Jones potential: When (not) to use it, Phys. Chem. Chem. Phys. **22**, 10624 (2020).

[80] See Supplemental Material http://link.aps.org/supplemental/10.1103/w7g3-6rsd for additional information and figures referenced in the text, which also includes Refs. [59,60,75,148–162].

[81] G. S. Wright, T. F. Watanabe, K. Amporndanai, S. S. Plotkin, N. R. Cashman, S. V. Antonyuk, and S. S. Hasnain, Purification and structural characterization of aggregation-prone human TDP-43 involved in neurodegenerative diseases, Iscience **23**, 101159 (2020).

[82] R. Haider, S. Penumutchu, S. Boyko, and W. K. Surewicz, Phosphomimetic substitutions in TDP-43's transiently α-helical region suppress phase separation, Biophys. J. **123**, 361 (2024).

[83] G. Krainer, T. J. Welsh, J. A. Joseph, J. R. Espinosa, S. Wittmann, E. de Csillery, A. Sridhar, Z. Toprakcioglu, G. Gudiškytė, M. A. Czekalska *et al.*, Reentrant liquid condensate phase of proteins is stabilized by hydrophobic and non-ionic interactions, Nat. Commun. **12**, 1085 (2021).

[84] Y. M. Ayala, P. Zago, A. D'Ambrogio, Y.-F. Xu, L. Petrucelli, E. Buratti, and F. E. Baralle, Structural determinants of the cellular localization and shuttling of TDP-43, J. Cell Sci. **121**, 3778 (2008).

[85] A. R. Tejedor, A. Garaizar, J. Ramírez, and J. R. Espinosa, RNA modulation of transport properties and stability in phase-separated condensates, Biophys. J. **120**, 5169 (2021).

[86] A. Garaizar, I. Sanchez-Burgos, R. Collepardo-Guevara, and J. R. Espinosa, Expansion of intrinsically disordered proteins increases the range of stability of liquid–liquid phase separation, Molecules **25**, 4705 (2020).

[87] M. Farag, S. R. Cohen, W. M. Borcherds, A. Bremer, T. Mittag, and R. V. Pappu, Condensates formed by prion-like low-complexity domains have small-world network structures and interfaces defined by expanded conformations, Nat. Commun. **13**, 7722 (2022).

[88] E. Pedraza, A. R. Tejedor, A. Feito, F. Gámez, R. Collepardo-Guevara, E. Sanz, and J. R. Espinosa, Predicting saturation concentrations of phase-separating proteins via thermodynamic integration, J. Chem. Theory Comput. **21**, 9919 (2025).

[89] A. Bremer, M. Farag, W. M. Borcherds, I. Peran, E. W. Martin, R. V. Pappu, and T. Mittag, Deciphering how naturally occurring sequence features impact the phase behaviours of disordered prion-like domains, Nat. Chem. **14**, 196 (2022).

[90] T. S. Harmon, A. S. Holehouse, and R. V. Pappu, Differential solvation of intrinsically disordered linkers drives the formation of spatially organized droplets in ternary systems of linear multivalent proteins, New J. Phys. **20**, 045002 (2018).

[91] J.-M. Choi, F. Dar, and R. V. Pappu, Lassi: A lattice model for simulating phase transitions of multivalent proteins, PLoS Comput. Biol. **15**, e1007028 (2019).

[92] C. S. Sørensen and M. Kjaergaard, Effective concentrations enforced by intrinsically disordered linkers are governed by polymer physics, Proc. Natl. Acad. Sci. USA **116**, 23124 (2019).

[93] J. A. Villegas, M. Heidenreich, and E. D. Levy, Molecular and environmental determinants of biomolecular condensate formation, Nat. Chem. Biol. **18**, 1319 (2022).

[94] S. K. Nandi, D. Österle, M. Heidenreich, E. D. Levy, and S. A. Safran, Affinity and valence impact the extent and symmetry of phase separation of multivalent proteins, Phys. Rev. Lett. **129**, 128102 (2022).

[95] C. P. Brangwynne, P. Tompa, and R. V. Pappu, Polymer physics of intracellular phase transitions, Nat. Phys. **11**, 899 (2015).

[96] H.-R. Li, W.-C. Chiang, P.-C. Chou, W.-J. Wang, and J.-r. Huang, TAR DNA-binding protein 43 (TDP-43) liquid–liquid phase separation is mediated by just a few aromatic residues, J. Biol. Chem. **293**, 6090 (2018).

[97] X. Yan, D. Kuster, P. Mohanty, J. Nijssen, K. Pombo-García, J. G. Morato, A. Rizuan, T. M. Franzmann, A. Sergeeva, A. M. Ly *et al.*, Intra-condensate demixing of TDP-43 inside stress granules generates pathological aggregates, Cell **188**, P4123 (2025).

[98] E. Pokrishevsky, M. G. DuVal, L. McAlary, S. Louadi, S. Pozzi, A. Roman, S. S. Plotkin, A. Dijkstra, J.-P. Julien, W. T. Allison *et al.*, Tryptophan residues in TDP-43 and SOD1 modulate the cross-seeding and toxicity of SOD1, J. Biol. Chem. **300**, 107207 (2024).

[99] D. Pantoja-Uceda, C. Stuani, D. V. Laurents, A. E. McDermott, E. Buratti, and M. Mompeán, Phe-Gly motifs drive fibrillization of TDP-43's prion-like domain condensates, PLoS Biol. **19**, e3001198 (2021).

[100] I. Sanchez-Burgos, A. R. Tejedor, A. Castro, A. Feito, R. Collepardo-Guevara, and J. R. Espinosa, Charged peptides enriched in aromatic residues decelerate condensate aging driven by cross-β-sheet formation, Nat. Commun. **16**, 8050 (2025).

[101] I. Sanchez-Burgos, L. Herriott, R. Collepardo-Guevara, and J. R. Espinosa, Surfactants or scaffolds? RNAs of varying lengths control the thermodynamic stability of condensates differently, Biophys. J. **122**, 2973 (2023).

[102] M. Farag, W. M. Borcherds, A. Bremer, T. Mittag, and R. V. Pappu, Phase separation of protein mixtures is driven by the interplay of homotypic and heterotypic interactions, Nat. Commun. **14**, 5527 (2023).

[103] K. Brown, P. Y. Chew, S. Ingersoll, J. R. Espinosa, A. Aguirre, A. Espinoza, J. Wen, K. Astatike, T. G. Kutateladze, R. Collepardo-Guevara *et al.*, Principles of assembly and regulation of condensates of polycomb repressive complex 1 through phase separation, Cell Rep. **42**, 113136 (2023).

[104] P. R. Banerjee, A. N. Milin, M. M. Moosa, P. L. Onuchic, and A. A. Deniz, Reentrant phase transition drives dynamic substructure formation in ribonucleoprotein droplets, Angew. Chem. **129**, 11512 (2017).

[105] A. Prakash, V. Kumar, A. Banerjee, A. M. Lynn, and R. Prasad, Structural heterogeneity in RNA recognition motif 2 (RRM2) of TAR DNA-binding protein 43 (TDP-43): Clue to amyotrophic lateral sclerosis, J. Biomol. Struct. Dyn. **39**, 357 (2021).

[106] L. M. Igaz, L. K. Kwong, Y. Xu, A. C. Truax, K. Uryu, M. Neumann, C. M. Clark, L. B. Elman, B. L. Miller, M. Grossman *et al.*, Enrichment of c-terminal fragments in tar DNA-binding protein-43 cytoplasmic inclusions in brain but not in spinal cord of frontotemporal lobar degeneration and amyotrophic lateral sclerosis, Am. J. Pathology **173**, 182 (2008).

[107] L. M. Igaz, L. K. Kwong, A. Chen-Plotkin, M. J. Winton, T. L. Unger, Y. Xu, M. Neumann, J. Q. Trojanowski, and V. M.-Y. Lee, Expression of TDP-43 C-terminal fragments *in vitro* recapitulates pathological features of TDP-43 proteinopathies, J. Biol. Chem. **284**, 8516 (2009).

[108] Y.-T. Wang, P.-H. Kuo, C.-H. Chiang, J.-R. Liang, Y.-R. Chen, S. Wang, J. C. Shen, and H. S. Yuan, The truncated C-terminal RNA recognition motif of TDP-43 protein plays a key role in forming proteinaceous aggregates, J. Biol. Chem. **288**, 9049 (2013).

[109] Y.-J. Zhang, Y.-F. Xu, C. Cook, T. F. Gendron, P. Roettges, C. D. Link, W.-L. Lin, J. Tong, M. Castanedes-Casey, P. Ash *et al.*, Aberrant cleavage of TDP-43 enhances aggregation and cellular toxicity, Proc. Natl. Acad. Sci. USA **106**, 7607 (2009).

[110] B. S. Johnson, J. M. McCaffery, S. Lindquist, and A. D. Gitler, A yeast TDP-43 proteinopathy model: Exploring the molecular determinants of TDP-43 aggregation and cellular toxicity, Proc. Natl. Acad. Sci. USA **105**, 6439 (2008).

[111] K. M. Kim, A. Girdhar, M. E. Cicardi, V. Kankate, M. Hayashi, R. Yang, J. L. Carey, C. M. Fare, J. Shorter, G. Cingolani *et al.*, NLS-binding deficient Kapβ2 reduces neurotoxicity via selective interaction with C9orf72-ALS/FTD dipeptide repeats, Commun. Biol. **8**, 2 (2025).

[112] M. P. Hughes, M. R. Sawaya, D. R. Boyer, L. Goldschmidt, J. A. Rodriguez, D. Cascio, L. Chong, T. Gonen, and D. S. Eisenberg, Atomic structures of low-complexity protein segments reveal kinked β sheets that assemble networks, Science **359**, 698 (2018).

[113] A. R. Tejedor, I. Sanchez-Burgos, M. Estevez-Espinosa, A. Garaizar, R. Collepardo-Guevara, J. Ramirez, and J. R. Espinosa, Protein structural transitions critically transform the network connectivity and viscoelasticity of RNA-binding protein condensates but RNA can prevent it, Nat. Commun. **13**, 5717 (2022).

[114] P. Robustelli, S. Piana, and D. E. Shaw, Developing a molecular dynamics force field for both folded and disordered protein states, Proc. Natl. Acad. Sci. USA **115**, E4758 (2018).

[115] K. Yamaguchi, J. Mima, K. Nakajima, H. Sakuta, K. Yoshikawa, and Y. Goto, Accelerated amyloid fibril formation

at the interface of liquid–liquid phase-separated droplets by depletion interactions, Protein Sci. **34**, e5163 (2025).

[116] M. Linsenmeier, L. Faltova, C. Morelli, U. Capasso Palmiero, C. Seiffert, A. M. Küffner, D. Pinotsi, J. Zhou, R. Mezzenga, and P. Arosio, The interface of condensates of the hnRNPA1 low-complexity domain promotes formation of amyloid fibrils, Nat. Chem. **15**, 1340 (2023).

[117] T. Das, F. K. Zaidi, M. Farag, K. M. Ruff, T. S. Mahendran, A. Singh, X. Gui, J. Messing, J. P. Taylor, P. R. Banerjee *et al.*, Tunable metastability of condensates reconciles their dual roles in amyloid fibril formation, Mol. Cell **85**, 2230 (2025).

[118] N. A. Erkamp, I. Sanchez-Burgos, A. Zhou, T. J. Krug, S. Qamar, T. Sneideris, E. Zhang, K. Nakajima, A. Chen, R. Collepardo-Guevara *et al.*, Dynamically arrested condensate fusion creates complex structures with varying material properties, bioRxiv 2024 (2024), https://doi.org/10.1101/2024.11.15.623768.

[119] A. R. Strom, A. V. Emelyanov, M. Mir, D. V. Fyodorov, X. Darzacq, and G. H. Karpen, Phase separation drives heterochromatin domain formation, Nature (London) **547**, 241 (2017).

[120] O. Sirozh, A. Saez-Mas, B. Jung, L. Sanchez-Burgos, E. Zarzuela, S. Rodrigo-Perez, I. Ventoso, V. Lafarga, and O. Fernandez-Capetillo, Nucleolar stress caused by arginine-rich peptides triggers a ribosomopathy and accelerates aging in mice, Mol. Cell **84**, 1527 (2024).

[121] P. Arosio, T. P. Knowles, and S. Linse, On the lag phase in amyloid fibril formation, Phys. Chem. Chem. Phys. **17**, 7606 (2015).

[122] A. Bhardwaj, M. P. Myers, E. Buratti, and F. E. Baralle, Characterizing TDP-43 interaction with its RNA targets, Nucl. Acids Res. **41**, 5062 (2013).

[123] E. Buratti and F. E. Baralle, TDP-43: Gumming up neurons through protein–protein and protein–RNA interactions, Trends Biochem. Sci. **37**, 237 (2012).

[124] Z. R. Grese, A. C. Bastos, L. D. Mamede, R. L. French, T. M. Miller, and Y. M. Ayala, Specific RNA interactions promote TDP-43 multivalent phase separation and maintain liquid properties, EMBO Rep. **22**, e53632 (2021).

[125] I. Sanchez-Burgos, J. R. Espinosa, J. A. Joseph, and R. Collepardo-Guevara, RNA length has a non-trivial effect in the stability of biomolecular condensates formed by RNA-binding proteins, PLoS Comput. Biol. **18**, e1009810 (2022).

[126] J. A. Joseph, J. R. Espinosa, I. Sanchez-Burgos, A. Garaizar, D. Frenkel, and R. Collepardo-Guevara, Thermodynamics and kinetics of phase separation of protein–RNA mixtures by a minimal model, Biophys. J. **120**, 1219 (2021).

[127] K. A. Burke, A. M. Janke, C. L. Rhine, and N. L. Fawzi, Residue-by-residue view of *in vitro* FUS granules that bind the C-terminal domain of RNA polymerase II, Mol. Cell **60**, 231 (2015).

[128] I. Alshareedah, T. Kaur, J. Ngo, H. Seppala, L.-A. D. Kounatse, W. Wang, M. M. Moosa, and P. R. Banerjee, Interplay between short-range attraction and long-range repulsion controls reentrant liquid condensation of ribonucleoprotein–RNA complexes, J. Am. Chem. Soc. **141**, 14593 (2019).

[129] J. C. Schwartz, X. Wang, E. R. Podell, and T. R. Cech, RNA seeds higher-order assembly of FUS protein, Cell Rep. **5**, 918 (2013).

[130] S. Matsui and R.-S. Nozawa, RNA impacts formation of biomolecular condensates in the nucleus, Biomed. Res. **42**, 153 (2021).

[131] J. E. Henninger, O. Oksuz, K. Shrinivas, I. Sagi, G. LeRoy, M. M. Zheng, J. O. Andrews, A. V. Zamudio, C. Lazaris, N. M. Hannett *et al.*, RNA-mediated feedback control of transcriptional condensates, Cell **184**, 207 (2021).

[132] A. Garaizar and J. R. Espinosa, Salt dependent phase behavior of intrinsically disordered proteins from a coarse-grained model with explicit water and ions, J. Chem. Phys. **155**, 125103 (2021).

[133] K. A. Lorenz-Ochoa, M. Cho, S. H. Parekh, and C. R. Baiz, Interaction-dependent secondary structure of peptides in biomolecular condensates, J. Am. Chem. Soc. **146**, 33616 (2024).

[134] C. Morelli, L. Faltova, U. Capasso Palmiero, K. Makasewicz, M. Papp, R. P. Jacquat, D. Pinotsi, and P. Arosio, RNA modulates hnRNPA1A amyloid formation mediated by biomolecular condensates, Nat. Chem. **16**, 1052 (2024).

[135] F. Ritossa, A new puffing pattern induced by temperature shock and DNP in drosophila, Experientia **18**, 571 (1962).

[136] A. Tissiéres, H. K. Mitchell, and U. M. Tracy, Protein synthesis in salivary glands of drosophila melanogaster: Relation to chromosome puffs, J. Mol. Biol. **84**, 389 (1974).

[137] M. R. Fernández-Fernández and J. M. Valpuesta, Hsp70 chaperone: A master player in protein homeostasis, F1000Research **7**, 1497 (2018).

[138] D. P. Kumar, C. Vorvis, E. B. Sarbeng, V. C. C. Ledesma, J. E. Willis, and Q. Liu, The four hydrophobic residues on the Hsp70 interdomain linker have two distinct roles, J. Mol. Biol. **411**, 1099 (2011).

[139] C. Hunt and R. I. Morimoto, Conserved features of eukaryotic Hsp70 genes revealed by comparison with the nucleotide sequence of human Hsp70, Proc. Natl. Acad. Sci. USA **82**, 6455 (1985).

[140] Y. Li, J. Gu, C. Wang, J. Hu, S. Zhang, C. Liu, S. Zhang, Y. Fang, and D. Li, Hsp70 exhibits a liquid-liquid phase separation ability and chaperones condensed FUS against amyloid aggregation, iScience **25**, 104356 (2022).

[141] H. Yu, S. Lu, K. Gasior, D. Singh, S. Vazquez-Sanchez, O. Tapia, D. Toprani, M. S. Beccari, J. R. Yates III, S. Da Cruz *et al.*, Hsp70 chaperones RNA-free TDP-43 into anisotropic intranuclear liquid spherical shells, Science **371**, eabb4309 (2021).

[142] I. Sanchez-Burgos, J. R. Espinosa, J. A. Joseph, and R. Collepardo-Guevara, Valency and binding affinity variations can regulate the multilayered organization of protein condensates with many components, Biomolecules **11**, 278 (2021).

[143] I. Sanchez-Burgos, J. A. Joseph, R. Collepardo-Guevara, and J. R. Espinosa, Size conservation emerges spontaneously in biomolecular condensates formed by scaffolds and surfactant clients, Sci. Rep. **11**, 15241 (2021).

[144] A. W. Folkmann, A. Putnam, C. F. Lee, and G. Seydoux, Regulation of biomolecular condensates by interfacial protein clusters, Science **373**, 1218 (2021).

[145] W. Voos and K. Röttgers, Molecular chaperones as essential mediators of mitochondrial biogenesis, Biochim. Biophys. Acta **1592**, 51 (2002).

[146] J. Gu, C. Wang, R. Hu, Y. Li, S. Zhang, Y. Sun, Q. Wang, D. Li, Y. Fang, and C. Liu, Hsp70 chaperones TDP-43 in dynamic,

liquid-like phase and prevents it from amyloid aggregation, Cell Research **31**, 1024 (2021).
[147] J. Wen, L. Hong, G. Krainer, Q.-Q. Yao, T. P. Knowles, S. Wu, and S. Perrett, Conformational expansion of Tau in condensates promotes irreversible aggregation, J. Am. Chem. Soc. **143**, 13056 (2021).
[148] A. P. Thompson, H. M. Aktulga, R. Berger, D. S. Bolintineanu, W. M. Brown, P. S. Crozier, P. J. in 't Veld, A. Kohlmeyer, S. G. Moore, T. D. Nguyen, R. Shan, M. J. Stevens, J. Tranchida, C. Trott, and S. J. Plimpton, LAMMPS—A flexible simulation tool for particle-based materials modeling at the atomic, meso, and continuum scales, Comput. Phys. Commun. **271**, 108171 (2022).
[149] T. Afroz, E.-M. Hock, P. Ernst, C. Foglieni, M. Jambeau, L. A. Gilhespy, F. Laferriere, Z. Maniecka, A. Plückthun, P. Mittl *et al.*, Functional and dynamic polymerization of the ALS-linked protein TDP-43 antagonizes its pathologic aggregation, Nat. Commun. **8**, 45 (2017).
[150] H. J. Berendsen, J. v. Postma, W. F. Van Gunsteren, A. DiNola, and J. R. Haak, Molecular dynamics with coupling to an external bath, J. Chem. Phys. **81**, 3684 (1984).
[151] F. J. Blas, L. G. MacDowell, E. de Miguel, and G. Jackson, Vapor-liquid interfacial properties of fully flexible Lennard-Jones chains, J. Chem. Phys. **129**, 144703 (2008).
[152] J. R. Espinosa, E. Sanz, C. Valeriani, and C. Vega, On fluid-solid direct coexistence simulations: The pseudo-hard sphere model, J. Chem. Phys. **139**, 144502 (2013).
[153] R. García Fernández, J. L. Abascal, and C. Vega, The melting point of ice I_h for common water models calculated from direct coexistence of the solid-liquid interface, J. Chem. Phys. **124**, 144506 (2006).
[154] J. R. Gissinger, B. D. Jensen, and K. E. Wise, Modeling chemical reactions in classical molecular dynamics simulations, Polymer **128**, 211 (2017).
[155] F. He, Y. Muto, M. Inoue, T. Kigawa, M. Shirouzu, T. Terada, and S. Yokoyama, Solution structure of RRM domain in TAR DNA-binding protein-43, PDB ID: 1WF0 (2004), https://doi.org/10.2210/pdb1wf0/pdb.
[156] P.-H. Kuo, C.-H. Chiang, Y.-T. Wang, L. G. Doudeva, and H. S. Yuan, The crystal structure of TDP-43 RRM1-DNA complex reveals the specific recognition for UG- and TG-rich nucleic acids, Nucl. Acids Res. **42**, 4712 (2014).
[157] A. Ladd and L. Woodcock, Triple-point coexistence properties of the Lennard-Jones system, Chem. Phys. Lett. **51**, 155 (1977).
[158] L. Lim, Y. Wei, Y. Lu, and J. Song, Als-causing mutations significantly perturb the self-assembly and interaction with nucleic acid of the intrinsically disordered prion-like domain of TDP-43, PLoS Biol. **14**, e1002338 (2016).
[159] S. Plimpton, Fast parallel algorithms for short-range molecular dynamics, J. Comput. Phys. **117**, 1 (1995).
[160] J. Ramírez, S. K. Sukumaran, B. Vorselaars, and A. E. Likhtman, Efficient on the fly calculation of time correlation functions in computer simulations, J. Chem. Phys. **133**, 154103 (2010).
[161] J. S. Rowlinson and B. Widom, *Molecular Theory of Capillarity* (Courier Corporation, North Chelmsford, MA, 2013).
[162] T. Schneider and E. Stoll, Molecular-dynamics study of a three-dimensional one-component model for distortive phase transitions, Phys. Rev. B **17**, 1302 (1978).
[163] http://www.hpc.cam.ac.uk
[164] https://www.archer2.ac.uk/
[165] http://www.upm.es
[166] https://www.cesvima.upm.es/services/hpc/magerit
[167] https://github.com/Reshiiiii/TDP-43_Data_Scripts